Oil Drilling Rig Diesel Power-plant Fuel Efficiency Improvement Potentials through Rule-Based Generator Scheduling and Utilization of Battery Energy Storage System

Danijel Pavković[*,1], Almir Sedić[2], and Zvonimir Guzović[1]

[1] Faculty of Mechanical Engineering and Naval Architecture, University of Zagreb,
Ivana Lučića 5, 10000 Zagreb, Croatia

[2] INA – Industrija nafte d.d., Avenija Većeslava Holjevca 10, 10000 Zagreb, Croatia

e-mails: danijel.pavkovic@fsb.hr; almir.sedic@ina.hr; zvonimir.guzovic@fsb.hr

Abstract

This paper presents the development of a rule-based energy management control strategy suitable for isolated diesel power-plants equipped with a battery energy storage system for peak load shaving. The proposed control strategy includes the generator scheduling strategy and peak load leveling scheme based on current microgrid active and reactive power requirements. In order to investigate the potentials for fuel expenditure reduction, 30 days-worth of microgrid power flow data has been collected on an isolated land-based oil drilling rig powered by a diesel generator power-plant, characterized by highly-variable active and reactive load profiles due to intermittent engagements and disengagements of high-power electric machinery such as top-drive, draw-works and mud-pump motors. The analysis has indicated that by avoiding the low-power operation of individual generators and by providing the peak power requirements (peak shaving) from a dedicated energy storage system, the power-plant fuel efficiency may be notably improved. An averaged power flow simulation model has been built, comprising the proposed rule-based power flow control strategy and the averaged model of a suitably sized battery energy storage system equipped with grid-tied power converter and state-of-charge control system. The effectiveness of the proposed rule-based strategy has been evaluated by means of computer simulation analysis based on drilling rig microgrid active and reactive power data recorded during the 30 day period. The analysis has indicated that fuel consumption of thus modified drilling rig diesel generator power-plant can be reduced by about 12% compared to current practice in the field relying on human operator-based decision making, which would also result in proportional reduction of carbon-dioxide emissions. Finally, the analysis has also shown that the return-of-investment period for the considered battery energy storage system might be between one and two years depending on the power-plant utilization (duty) ratio.

Keywords: Oil drilling rig microgrid; Diesel power-plant; fuel efficiency; energy management; battery energy storage; return-of-investment period.

[*] Corresponding author

1. Introduction

Meeting the society's energy needs, which are still being predominantly accommodated from fossil fuel sources, has become a paramount task for energy policy makers due to fluctuating oil and gas prices. Even though rising oil and gas prices stimulate new reserves discovery and their enhanced recovery [1], the non-renewable nature of those resources mandate that at certain point their peak production potential is going to be reached [2]. Hence, numerous efforts have been undertaken by major oil/gas industries in order to improve the efficiency of the complete hydrocarbon production chain from exploration (drilling), through extraction and crude product transportation, and final processing and refining, as indicated by recent sustainability reports published by Statoil [3] and British Petroleum [4]. The aforementioned efforts may include system-wide measures aimed at reducing the overall carbon footprint by means of fugitive methane emissions mitigation strategies [5], and adopting low-carbon technologies such as carbon capture and off-shore wind [3], thus improving the respective stakeholders' carbon trade balance. Making use of drilling technologies advances [6] has also been recognized as a potential factor in increasing oilfield production capacities and drilling operation cost-effectiveness. The aforementioned practices should be augmented at the operational (production) level by adopting appropriate energy efficiency improvement measures, such as drilling facility power-plant waste heat capture and energy storage [7], which can facilitate notable fuel savings and carbon-dioxide (CO_2) emissions reductions on off-shore drilling rigs. Since the current number of readily available land-based drilling rigs exceeds the number of those for off-shore drilling operations approximately four-fold [8], it would also be worthwhile to investigate land-based rigs' fuel expenditure and CO_2 emissions reduction potentials via appropriate energy management strategies.

The schematic layout of the land-based oil drilling rig alternating-current (AC) microgrid is illustrated in Fig. 1. It is typically powered by a diesel generator-based power-plant [9], and characterized by high-magnitude load variations due to frequent engagement and variable-power operation of mud pumps, draw-works hoist and "top-drive" drilling electrical machines. In addition, the drilling rig microgrid may be characterized by high reactive power requirements, especially for "mature" drilling rig variable speed drives (VSD) utilizing thyristor-based power converters and series-excitation direct-current (DC) machines [10] (see discussions in Sections 2 and 3). The aforementioned power variations, especially those occurring during drill-string fitting and drill bit exchange, borehole stabilization (via casings insertion and wall cementing), and directional drilling operations (see e.g. [9]), are typically covered by bringing additional generators on-line, which results in increased fuel expenditures. Hence, it would be worthwhile to analyze the operation of the drilling rig power-plant and adjacent microgrid for typical operating scenarios, in order to find appropriate measures for fuel expenditure reduction. These may include appropriate generator scheduling techniques and related microgrid hybridization in terms of including an additional electrical energy storage (dotted path in Fig. 1), which may also be used as a backup/emergency power source in case of power-plant shutdown. As indicated in [11], drilling rig power grid retrofitting and modernization measures typically

comprise a fraction of brand-new drilling rig cost, which might make these upgrades palatable to small-to-medium oil and gas drilling companies operating "mature" drilling equipment.

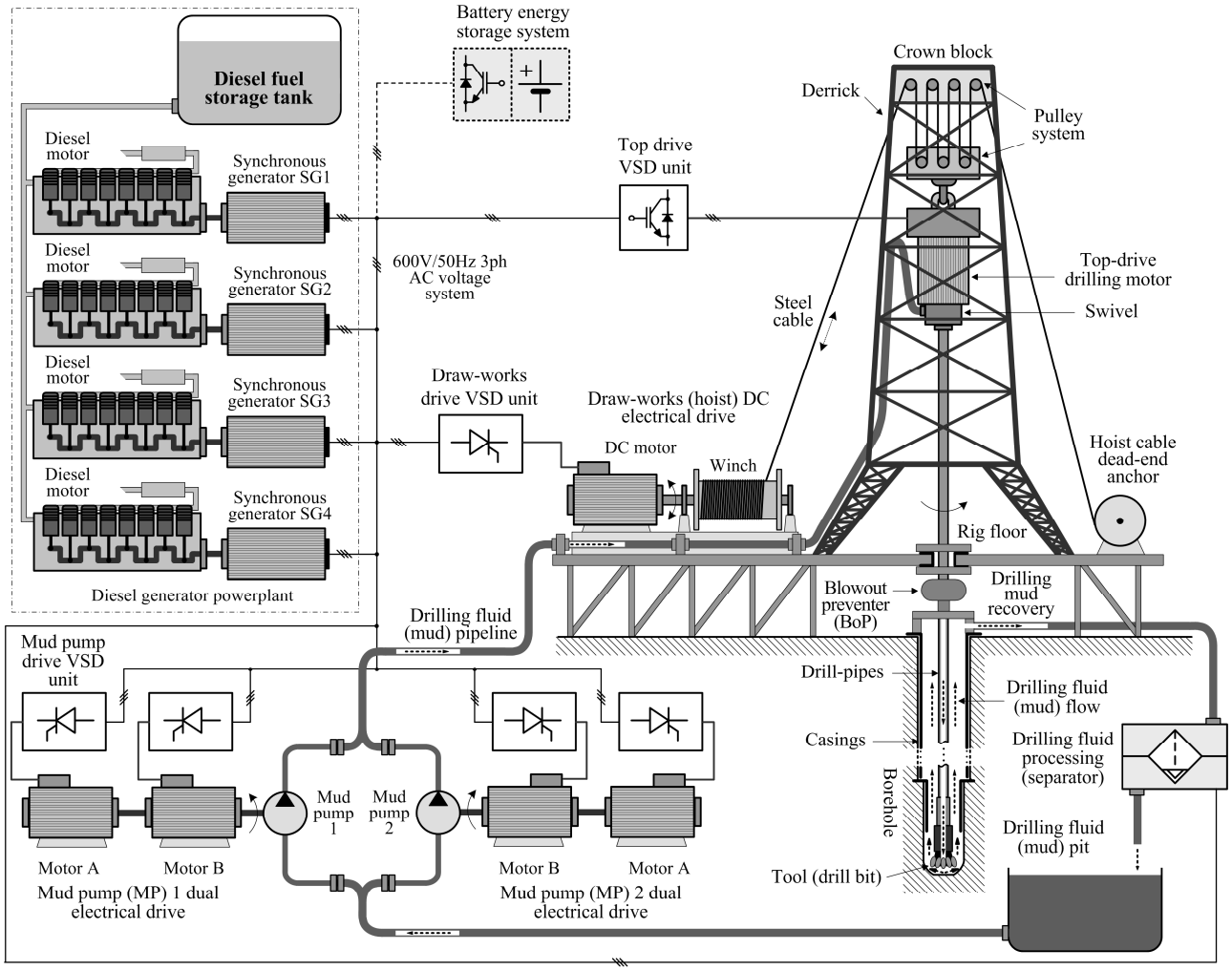

Figure 1. Schematic layout of a land-based oil-drilling rig.

Moreover, the aforementioned microgrid hybridization measures may also have a broader scope, because internal combustion (e.g. diesel) engine-based power-plants may account for up to 15% of the total installed capacity worldwide [12], either as primary power sources of isolated (islanded) power grids (such as oil drilling rig microgrid being the subject of case study herein), or as backup plants for essential businesses and services, such as hotels, airports, hospitals, and those industries that require reliable power at all times. Since the operation of diesel power-plant is typically associated with rather substantial fuel transportation costs [13], notable research efforts have been dedicated to optimization of diesel power-plant fuel efficiency. Recent research has shown that meta-heuristic search algorithms can be used to find the optimum number of generators [14] which minimizes the specific power plant fuel consumption. Due to their simplicity, rule-based control strategies are frequently used in real-time energy management applications aimed at coordination of multiple power sources, as shown for the case of an isolated AC microgrid based on a diesel power-plant and photovoltaic (PV) system supported by battery energy storage [15].

Namely, the aforementioned energy management task is similar to hybrid electric vehicle power-plant control aimed at minimizing fuel consumption along with simultaneous coordination with the vehicle propulsion (drivetrain) [16], which can be facilitated by means of an appropriate rule-based control strategy [17]. Integration of renewable energy sources may offer additional benefits in terms of diesel-based isolated microgrid fuel efficiency improvement. An example of diesel power-plant integration with a hydro-accumulation power plant and battery energy storage has been presented in [13], wherein significant fuel expenditure reduction has been achieved. Similar economic benefits of augmenting the diesel power-plant with a wind turbine-based power source have been reported in [18]. Reference [19] presents the case of diesel power-plant equipped with battery energy storage and combination of PV and wind-based renewable energy sources with detailed analysis of battery life cycle costs and overall performance analysis of such a complex power system.

In order to meet the required load leveling and peak shaving performance of such hybrid microgrids, suitable low-level control strategies, aimed at maintaining prescribed voltage and frequency of the AC microgrid are typically included within the battery energy storage system power converter [20]. Different energy storage and power converter topologies for microgrid auxiliary power supplies have been compared in [21]. Moreover, the battery energy storage system needs to be designed with sufficient energy storage capacity for the anticipated discharge regimes [22], while the grid-side power converter interface needs to be dimensioned based on the expected peak power demand [23]. The required storage capacity and choice of suitable battery technology is typically based on the analysis of time-varying load profiles [24]. A comprehensive statistical analysis of long-term available wind energy, presented in [25], has been used for the optimization of energy storage capacity within a standalone wind energy system. On the other hand, the short-term intermittence of available wind power in an isolated small-scale high-altitude wind energy system [26] has been analyzed and used for energy storage system dimensioning aimed at achieving steady energy delivery to the power grid. In the case of larger energy systems subject to daily and weekly power fluctuations, particular attention needs to be given to battery energy storage system capacity and power ratings [27]. On the other hand, the anticipated energy storage operating regimes, i.e. peak (pulsed) load leveling or steady power delivery, represent the key criteria for the choice of suitable battery energy storage technology [28]. These battery system design measures should also ensure that deep battery discharging operation would be prevented in order to avoid accelerated battery aging issues [29].

Unsurprisingly, the aforementioned power system hybridization measures have started to appeal to oil/gas drilling and supporting enterprises, as well. One such example is the innovative diesel engine + fuel cell off-shore platform supply vessel design with clear fuel efficiency improvement potential [30]. Moreover, off-shore drilling facility power grid reliability and efficiency improvement through adopting hybrid AC/DC distribution systems have been analyzed in [31]. In that regard, on-shore drilling rigs retrofitting with active power filters has been researched in [32] aimed at improving the grid power quality and reducing grid harmonics power losses. Additional efforts related to drilling operations efficiency improvement may also include harnessing the regenerative braking operation of the draw-works hoist drive during drill-string descending phase

[33]. However, inclusion of a dedicated peak shaving/load leveling battery energy storage system, and development of related hybrid power system control strategy aimed at oil drilling rig fuel efficiency improvement and carbon emission reduction have not been discussed in the available literature.

To this end, this paper proposes a rule-based scheduling scheme for a diesel power-plant and a related energy management control strategy based on the utilization of an appropriate battery energy storage system for peak load shaving purposes. In particular, the hypothesis of this work is that by changing the manner of energy management in the isolated microgrid through the improvement in diesel generator turn-on/turn-off scheduling, along with the inclusion of sufficient-capacity battery energy storage system equipped with grid-tied inverter for peak load shaving purposes, a notable reduction of energy (diesel fuel) consumption and greenhouse gasses emissions can be achieved in comparison to current practices relying on human expert-based decision making. The basis for the control strategy design and corresponding energy storage system sizing has been obtained by analyzing the load profiles of the diesel generator power-plant within the isolated oil drilling rig AC microgrid, characterized by highly-variable active and reactive power requirements. The proposed energy management control strategy has been implemented in Matlab/Simulink simulation environment within a simplified power flow-based microgrid model. In comparison with previous research efforts in similar hybrid power systems, which have employed (i) dynamic cooperative control between microgrid power sources [20], (ii) meta-heuristic optimization applied to generator scheduling [14], and (iii) on-line optimization of battery state-of-charge and fuel consumption [16], the proposed energy management control strategy offers some distinct advantages. Namely, it is characterized by simple implementation and straightforward tuning, due to its being based on purely algebraic calculations of additional (peak shaving) microgrid power requirements. Moreover, it is characterized by modularity and hierarchical structure, wherein the microgrid power demand is determined by the higher-level power allocation rule-based strategy, which assigns the required number of generators on-line and commands the battery energy storage system discharging during peak power demand intervals. Finally, the proposed simulation model utilizing field data recorded under realistic operating and load conditions may be useful for the assessment of fuel savings and return-of-investment period for diesel power-plants employing an additional energy storage system, along with the associated CO_2 emission reduction potentials.

The paper is organized as follows. Section 2 outlines the land based drilling rig facility and provides key description and parameters of main drilling rig microgrid loads. The proposed diesel generator-based microgrid control methodology has been outlined in Sections 3 and 4, wherein Section 3 presents the results of analysis of microgrid power requirements and generator fuel expenditures, and related battery energy storage system sizing study, while Section 4 presents the rule-based generator scheduling control strategy incorporating the peak shaving based on battery energy storage system power flow control, and battery state-of-charge control system design. Section 5 presents the results of simulation verification of the proposed energy management control strategy, along with the related discussion on the estimated diesel fuel expenditure and

CO_2 emission reduction, and battery energy storage system effectiveness and the expected return-of-investment period. The main results and conclusions are summarized in Section 6, which also provides guidelines for future work.

2. Facility operation overview

The particular land-based oil drilling rig, depicted by the schematic representation in Fig. 1, is powered by diesel engine-based synchronous generator power-plant comprising four generator units. Individual generators intended for supplying the local 600V/50 Hz three-phase AC electrical microgrid are rated with apparent power S_N = 875 kVA and power factor $\cos\varphi_N$ = 0.8 (700 kW/525 kVAr nominal active and reactive power), and 1000 rpm rated speed [34]. The drilling rig microgrid is characterized by numerous high-power loads, such as electrical drives powering dual drilling fluid (drilling mud) pumps, drilling hoist (draw-works) electrical drive, top-drive speed-controlled drilling motor and drilling mud processing plant. The draw-works and mud-pump speed-controlled electrical drives are mature DC drives equipped with thyristor-based AC/DC power converters, where the draw-works drive (750 kW rated power) is based on a separately-excited DC machine, while each dual mud pump drive is powered by two series-excitation DC machines with 660 kW power ratings. Finally, the drilling motor within the top-drive needs to facilitate high-power and low-speed operation in excess of 600 kW, typically operating below 250 rpm. A variable speed drive (VSD) based on AC or DC electric motor is typically used for that purpose, thus facilitating favorable dynamics and straightforward implementation of advanced drilling control functions such as drill-string torsional vibrations active damping system (see e.g. [35] and references therein).

During normal drilling operations, characterized by approximately constant drilling motor and mud pump drive load and draw-works operating at low-power settings, the power plant load is rather low and does not vary significantly, so a reduced number of generators (typically two for redundancy purposes) can provide the drilling rig power supply (see discussion in next section). On the other hand, under unfavorable operating conditions, such as in the case of emphasized drill-bit stick-slip motion and directional drilling operations, the top drive load significantly increases due to high-magnitude torsional vibrations and increase in drill-string vs. borehole sidewall interactions. Moreover, borehole rimming, casings insertion and drill bit exchange need to be periodically performed in order to improve the drilling process quality and ensure safe operation [9], consequently resulting in increased power plant load variations due to draw-works hoist being intermittently loaded near full power. Finally, the speed-controlled series DC motor-based pump drives operating at the fraction of rated power can be characterized by predominant reactive power requirements with respect to AC grid [36]. Hence, in order to avoid AC grid frequency or voltage instability under aforementioned harsh microgrid operating regimes, additional generators are brought on-line and operated near or above the optimal power factor ($\cos\varphi \approx 0.8$) in the case of predominant active power requirement, while in the reactive power-intensive scenarios the power factor may be reduced well below the rated value ($\cos\varphi < 0.8$) by means of increased generator excitation.

3. Results of field data analysis

This section presents the results of drilling rig AC microgrid load profile recording over a 30-day period, and illustrates specific load behavior for different operating regimes. Based on the analysis of averaged power-plant output, and assuming ample energy storage capacity during peak power requirements, the minimum number of generators is determined under "ideal" load preview conditions. These results are then used to assess the potential for diesel fuel savings, and as a basis for the configuration and sizing of the dedicated battery-based energy storage system.

3.1. Illustration of microgrid load variability

Drilling rig microgrid data have been continuously collected with a sampling rate of 0.2 Hz (sampling period $T = 5$ s) over the 30-day period characterized by directional drilling operations at depths below 1850 m. This resulted in about 518400 data points per individual recorded microgrid variable, covering a wide range of drilling rig microgrid load variations and operating regimes. Data collection included key variables from dedicated control units of power-plant generators and major loads, which were connected to the mutual ProfiBus network, and an industrial PC computer running proprietary data acquisition software used as signal acquisition platform. The collected data included diesel generator power-plant key electrical quantities, i.e. statuses of individual generators (on-line or turned off), and individual generator line voltage and current, and power factor. The electrical quantities (voltage/current) of all major loads, i.e. mud pumps, draw-works and top drive drilling motor electrical drives have been measured as respective DC values at individual power converters' DC link sides.

Figure 2 shows the key recorded electrical data for the diesel generator power-plant (top row), mud pump electrical drives (mid row) and draw-works hoist and top drive drilling motor (bottom row) over a 48 hour period of directional (slanted) drilling operations during which the drilling rig has been subjected to the following regimes: (i) drilling (time-stamps from 30 to 43 h), (ii) drilling with periodic bore-hole rimming, characterized by low-power top drive operation and high-power intermittent draw-works hoist operation intervals (time-stamps from 43 to 64h), and predominant drilling with sporadic draw-works engagement for borehole rimming purposes (time stamps from 64 to 78h). The results in Fig. 2 confirm that the diesel power plant is subjected to highly variable loads during rimming operations, i.e. when the draw-works drive intermittently operates under high load. During regular drilling (draw-works is under low load), the drilling rig microgrid is also characterized by quasi-steady-state load, which is largely due to top-drive operating at approximately constant load, and rather large steady load produced by mud pumps. During the observed period, typically three generators have been operational under high load conditions corresponding to drilling and mud pump constant-power operation, with the average power-plant power factor close to the rated value ($\cos\varphi = 0.8$). On the contrary, during rimming operations, wherein the draw-works is predominantly used (with pumps off-line), two diesel generators have been able to support the

local power grid, which has been subjected to notable reactive power requirement from the thyristor-based draw-works drive power converter. This mandated generator operation at power factor values lower than rated ones, especially emphasized for generator unit SG1 during rimming operations (see 42 – 66h interval in Fig. 2). Moreover, it can also be observed that for the particular example all generators have been operating well below their rated power, even during peak power loads.

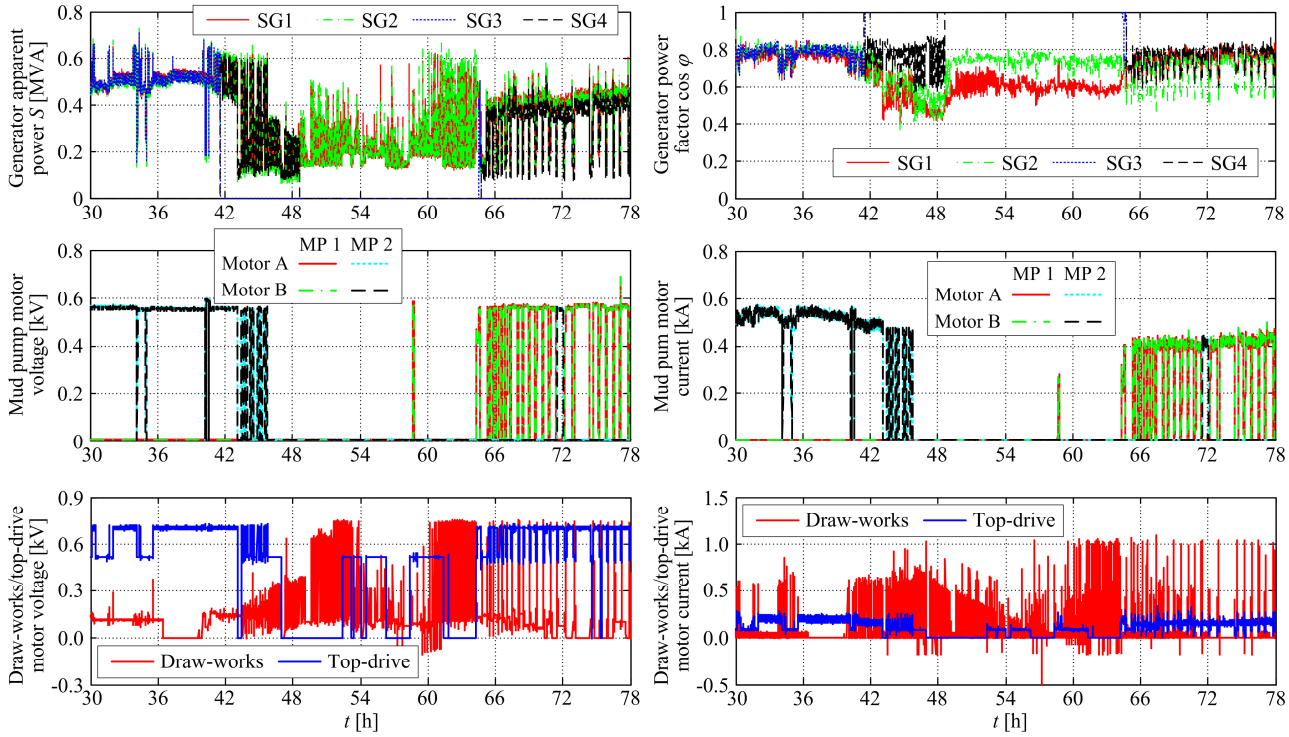

Figure 2. Synchronous generator apparent power and power factor, and mud pump, top drive and draw-works voltage and current measurements during 48 h of directional drilling operation of drilling rig in question.

3.2. Power-plant load and energy storage requirement analysis

Based on the aforementioned insights, it would be of interest to analyze the average and peak power requirement of the drilling rig microgrid over the whole 30-days worth field data, in order to reveal the possibilities for improvement of the diesel power-plant operation in terms of better utilization of individual generators' operating range. For this purpose, microgrid apparent, active and reactive power measurements have been averaged by an adaptive Kalman filter [37], which is characterized by favorable tracking ability and good suppression of steady-state "noise" (see Appendix A).

Figure 3 shows the comparative instantaneous and averaged apparent, active and reactive power traces over the observed 30-day (720 h) period, as well as the actual number of running generators in the field. The power traces in Fig. 3 indicate that the drilling rig is subject to relatively large power demands (apparent power demand frequently reaches 2 MVA), and large and prolonged instantaneous power variations with respect to comparative averaged power traces, which, in the case of reactive power demand, may periodically fluctuate up to 1 MVAr for up to 30 h. The histogram plots (distributions) of active,

reactive and apparent power and number of actually running power-plant generators in Fig. 3 additionally confirm that the presented data cover for a relatively wide range of power-plant (microgrid) power demands associated with different number of generators on-line. It can also be noted that a notable portion of microgrid operating regimes is characterized with either a rather high or rather low load, with median loads being somewhat less represented in the overall data set. This further confirms that the microgird load is rather variable in nature and can take on a wide range of active/reactive power values.

Averaged microgrid apparent power may provide a good insight into the steady power demand, so these data may be used to ascertain the minimum number of generators required for the grid quasi-steady-state load. Since grid power variations, especially large peak loads, may result in grid voltage and frequency instability, it is assumed that any peak load demands beyond the generator ratings would be eventually dealt with by an appropriately sized energy storage system (Section 4). Moreover, it is assumed that in the aforementioned hypothetical scenario all generators would be operating with the same power factor value, wherein the reactive and active power delivery to the grid may be provided up to individual generator active and reactive power ratings. This straightforward rule-based generator control strategy should be easily implementable because synchronous generators' active and reactive power controls are effectively decoupled through diesel engine power output (at grid frequency-fixed engine speed), and generator excitation control action.

Based on the above assumptions, the number of generators required to cover for the averaged apparent microgrid load can be estimated as the ratio between the averaged microgrid power demand (obtained from generator field data) and individual generator apparent power rating S_N, rounded towards the larger integer (ceiling) value:

$$\hat{N}_{SG}(k) = ceil\left[\frac{1}{S_N}\sum_{i=1}^{4}\overline{S}_i(k)\right], \tag{1}$$

where $N = 4$ is the number of power-plant generators, $i = 1 \ldots 4$ is the generator number (SG1 … SG4 in Fig. 1), and $\overline{S}_i(k)$ is the averaged value of i-th generator apparent power at k-th time step (time instant $t = kT$).

The number of generators required to deal with the averaged microgrid apparent power load, estimated according to (1), is also shown in Fig. 3. The result clearly indicates that it would be possible to operate the drilling rig microgrid with a reduced number of generators (up to two less generators running) and with similar number of generator switch-on/switch-off events (around 30) when compared to the current practice in the field. Moreover, by reducing the number of generators the useful generator power range would be better utilized, instead of the empirical scheme implemented in the field, wherein individual generators are frequently operated at the fraction of their nominal power (cf. Fig. 2 and related discussion).

However, in order to implement the proposed generator scheduling scheme, it would be necessary to supply the excess power (load) from the adequate energy storage system with sufficient active and reactive power delivery capacity. Hence, it is also crucial to analyze the peak active, reactive, and apparent power profiles obtained by using the aforementioned generator scheduling scheme. Based on the assumption that individual generators may be loaded up to their respective active

and reactive power ratings, the excess power (i.e. peak loads) which would not be supplied by the previously determined minimum number of generators ($\hat{N}_{SG}$) is estimated as follows:

$$\Delta P(k) = \begin{cases} 0 \ \text{ for } \ \sum_{i=1}^{4} P_i(k) \le \hat{N}_{SG}(k) P_N, \\ \sum_{i=1}^{4} (P_i(k)) - \hat{N}_{SG}(k) P_N \ \text{ for } \ \sum_{i=1}^{4} P_i(k) > \hat{N}_{SG}(k) P_N, \end{cases} \tag{2}$$

$$\Delta Q(k) = \begin{cases} 0 \ \text{ for } \ \sum_{i=1}^{4} Q_i(k) \le \hat{N}_{SG}(k) Q_N, \\ \sum_{i=1}^{4} (Q_i(k)) - \hat{N}_{SG}(k) Q_N \ \text{ for } \ \sum_{i=1}^{4} Q_i(k) > \hat{N}_{SG}(k) Q_N, \end{cases} \tag{3}$$

$$\Delta S(k) = \sqrt{\Delta P^2(k) + \Delta Q^2(k)} \ . \tag{4}$$

where ΔP, ΔQ, and ΔS are microgrid total active, reactive and apparent excess power demands with respect to minimum number of required generators, P_i and Q_i (i = 1 … 4) are instantaneous active and reactive power requirements obtained from field data, and P_N and Q_N are individual generator active and reactive power ratings (Section 2).

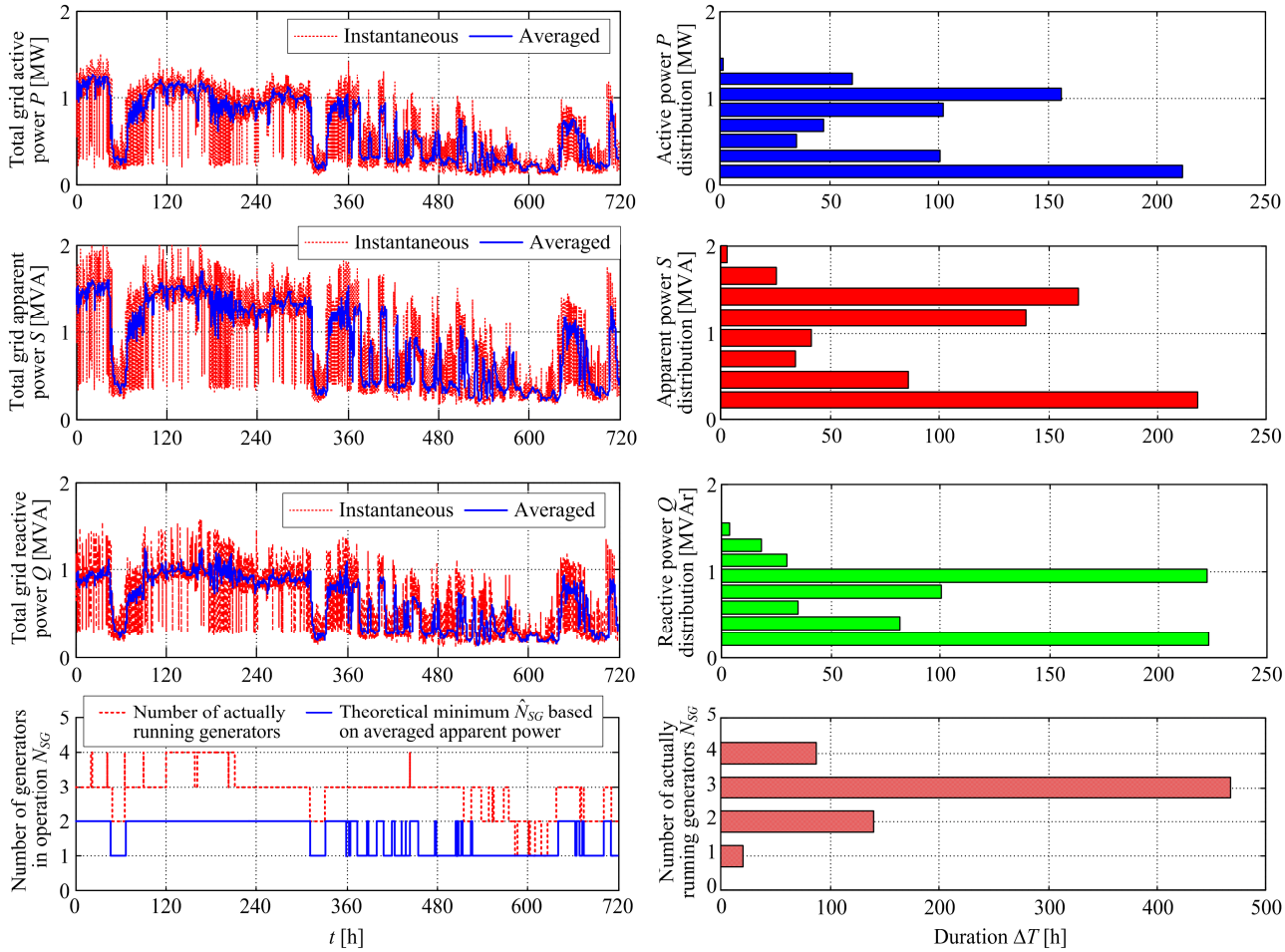

Figure 3. Instantaneous and averaged power delivery of the diesel generator power-plant and number of running generators for the observed 30-day period, and corresponding histograms (distributions), along with theoretical number of generators required if energy storage system is used.

Top plot in Fig. 4 shows the microgrid excess power profiles estimated according to expressions (2) – (4) assuming a reduced number of generators according to (1). It is apparent that under the observed microgrid load conditions, the excess load with reduced number of running generators would be predominantly due to observed large variations of the reactive power. This is further confirmed by excess active, reactive and apparent power histograms, shown in bottom plots in Fig. 4. Namely, cumulative durations of excess reactive power requirements ΔQ are approximately four-fold larger than respective durations of active power ΔP requirements, and, hence, reactive power excess ΔQ predominates within the estimated excess apparent power ΔS. Moreover, excess apparent power ΔS, which would need to be covered by the energy storage system (apparent power limit) does not exceed 0.6 MVA, while the active power requirements (related to energy storage capacity and discharge duration) reach up to 0.4 MW.

Figure 5 shows the energy discharge requirements during active power peak loads shown in Fig. 4. In particular, 72 distinct discharging events have been indicated which might be used to assess the prospective energy storage system capacity (Section 4). The results show that for the considered excess active loads, the energy storage would have to provide up to ΔW_{max} = 94 kWh of energy storage capacity in the worst-case scenario considered in this analysis. Durations of individual requested discharge events, also shown in Fig. 5, indicate that the required discharge duration of the energy storage system would not exceed one hour for the considered generator rule-based scheduling scenario.

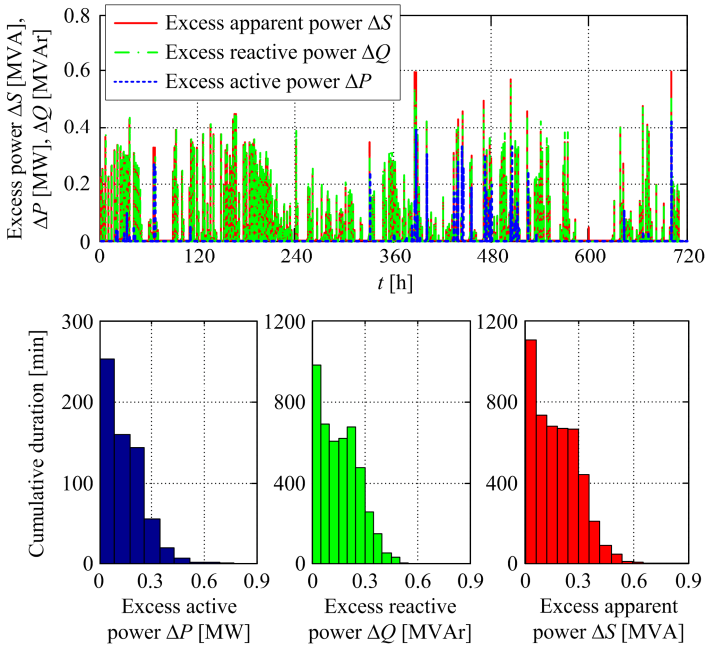

Figure 4. Traces of excess power requirements from the energy storage system, and power vs. time duration histograms for the observed 30-day period of drilling rig operation.

Since electrochemical batteries are considered for energy storage, deep discharges should be avoided in order to prolong the battery energy storage system useful cycle life [29], which is typically inversely proportional to the average depth-of-

discharge during battery calendar life. Hence, the aforementioned energy storage requirement ΔW_{max} should be augmented in the following way [26]:

$$W_{st} = \frac{\Delta W_{max}}{1 - \xi_{min}} . \quad (5)$$

in order to ensure that the battery state-of-charge ξ would be kept above the predefined minimum value ξ_{min} even during the worst-case discharging scenario, thus effectively limiting the battery depth-of-discharge δ for the anticipated discharge regimes:

$$\delta \le \delta_{max} = 1 - \xi_{min} . \quad (6)$$

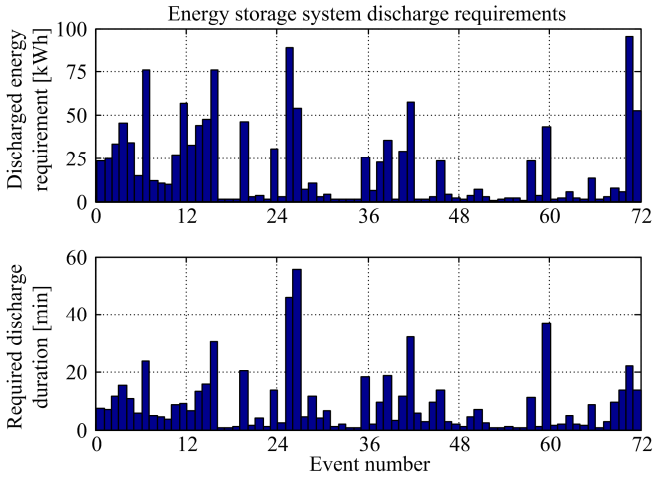

Figure 5. Hypothetical energy storage system discharge requirements.

3.3. Estimated power-plant fuel consumption

Generator active power output vs. fuel consumption rate relationship shown in Fig. 6 has been used for the purpose of evaluating the power-plant fuel consumption. The fuel rate characteristic (solid curve in left-hand-side plot in Fig. 6) has been obtained by interpolating the diesel generator manufacturer's data [34] (denoted by "*" symbols) by a cubic polynomial curve. Since fuel consumption rate data near idling point (P = 0) were not provided by the manufacturer, the cubic interpolation characteristic has been extrapolated towards zero, where it exhibits a more pronounced curvature compared to higher generator output power settings. This corresponds to the increase of specific fuel consumption rate at low output power, as illustrated in right-hand side plot in Fig. 6, which is in agreement with the results reported in [14]. Since higher specific fuel consumption can be expected during generator low power operation and vice versa, it would be sensible to avoid generator operation at low active power output.

The results of estimation of cumulative fuel consumption for individual generators and the estimated overall power-plant fuel consumption[†] based on generator power output data are shown in Fig. 7. The output active power and cumulative

[†] Being subject to confidentiality restrictions, the actual drilling rig fuel expenditures could not be released.

fuel consumption estimates (top and middle plot in Fig. 7) show that generators SG1 through SG3 have been periodically cycled in order to achieve approximately the same levels of utilization, presumably to meet approximately the same maintenance cycle requirements (see e.g. [38]). On the other hand, the fourth generator (SG4) utilization has been about half the utilization of SG1 – SG3 during the observed 30-day period. By summing up the individual contributions of generators SG1 – SG4, the overall power-plant estimated fuel consumption at the end of 30-day period has amounted to 146.73 m^3 of diesel fuel. The aforementioned cumulative fuel consumption is going to be used as a benchmark for the power-plant energy management system simulation analysis presented in the next section.

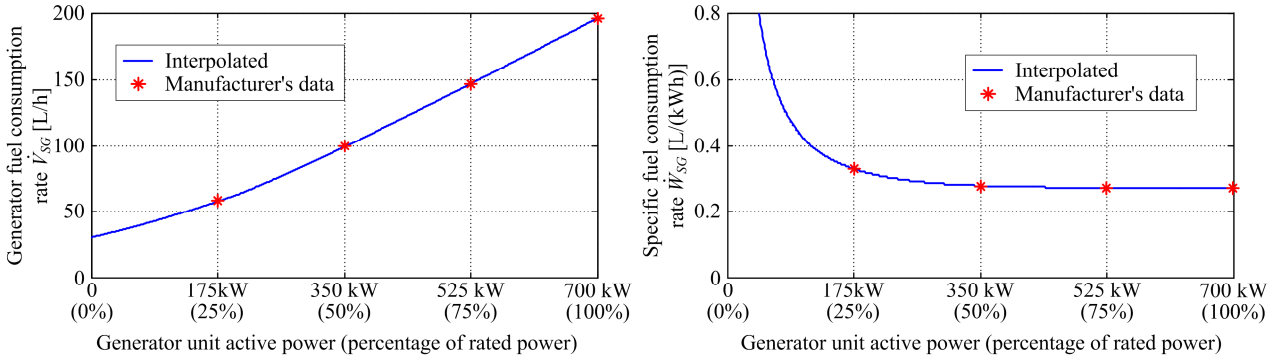

Figure 6. Diesel generator fuel consumption rate data and specific consumption obtained from manufacturer [34], with cubic polynomial-based approximation curve suitable for fuel consumption estimation.

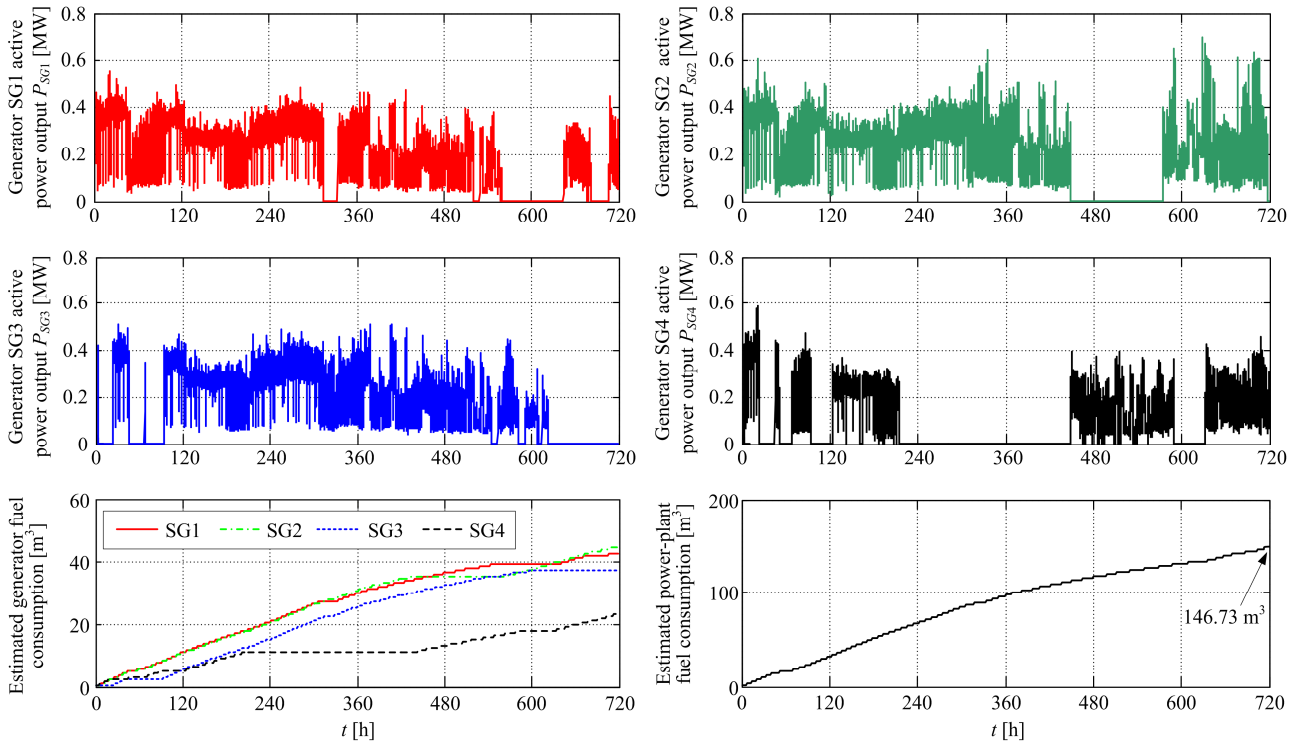

Figure 7. Comparative generator active power traces, and estimates of individual generator and overall power-plant fuel consumption over the 30-day period.

3.4. Proposed battery energy storage system arrangement, parameterization and costs

Due to specific requirements of land-based drilling rigs, the energy storage system ought to be robust, compact and easily transportable, and characterized by inherently high operational safety. Since automotive batteries intended for electric vehicle use ought to satisfy the aforementioned requirements as well [39], a suitably chosen automotive battery technology can be adopted for the proposed application. The lithium-iron-phosphate ($LiFePO_4$) battery technology currently represents a promising choice in terms of high power density and operational safety, while also being characterized by relatively moderate costs with respect to energy storage capacity [39]. Moreover, these batteries are also characterized by rather high durability in terms of battery cycle life as reported in [40]. In particular, over 2000 charging/discharging cycles can be achieved with 80% average depth-of-discharge per cycle during useful service life according to manufacturer's data [41]. Assuming the aforementioned worst-case scenario with 80% battery depth-of-discharge (ξ_{min} = 20%), for the considered maximum observed discharge requirement ΔW_{max} of 94 kWh, the adjusted battery energy storage capacity according to (5) would equal W_{st} = 117.5 kWh.

The considered battery system would also need to be equipped with as suitably sized three-phase power converter (inverter) in order to enable battery connection and power supply to the drilling rig AC microgrid. Figure 8 shows the prospective energy storage system arrangement, comprising a battery (denoted by its equivalent electric circuit) directly connected to the DC link of the three-phase two-level switching inverter [23] equipped with grid-side harmonic LCL filter [43], which is required to reduce the total harmonic distortion (THD) due to inverter switching action to an acceptable level, and, thus, to provide favorable quality of the power delivered to the drilling rig microgrid [32]. In addition, the grid inverter may also include a neutral line balancing control system in the case of perceptible load asymmetry conditions [43]. The power flow control system within the inverter is typically implemented in the so-called grid synchronous (d-q) reference frame (see e.g. [23]). In this way, controlled delivery of energy storage system reactive power Q_{ESS} to the grid can be fully-decoupled from the active power flow P_{ESS} bidirectional control (needed for periodic battery recharging after peak active load-related discharging events). The active and reactive power references during peak load events can be calculated within the framework of voltage/frequency droop control [42], while the corresponding low-level current control can be based on respective direct (d) and quadrature (q) proportional-integral current controllers [43].

For the aforementioned battery capacity requirement of 117.5 kWh, the battery system specific cost is estimated in [44] to 850 EUR/kWh, which amounts to approximately 100000 EUR for the particular battery system. Note, however, that the actual cell costs would amount to about half of the aforementioned cost, whereas the remainder would include battery management system (BMS) power electronics and control hardware, as well as battery housing, thermal management system, wiring and various accessories [39]. The aforementioned battery management and diagnostics systems and

auxiliaries are essential for correct battery system operation under rather harsh exploitation conditions encountered in automotive and electrical power system applications [45].

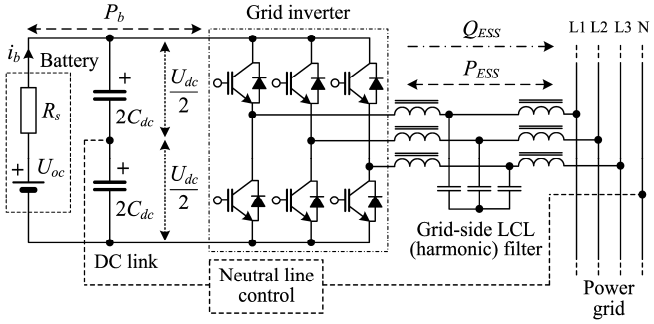

Figure 8. Principal schematic of battery-based energy storage system equipped with three-phase grid power converter (inverter) suitable for peak load shaving application.

The inverter apparent power rating requirement of 0.6 MVA, obtained by the peak load analysis in previous subsection, has been used to estimate the inverter cost. According to [44], the median battery inverter specific cost for lithium battery applications is estimated to 125 EUR/kVA of installed inverter power, which results in power inverter investment costs of 75000 EUR for a 0.6 MVA system. Finally, additional 19 EUR/kVA per year would be required for the operational and maintenance costs for the considered energy storage system [44], which results in additional cost of 11400 EUR/year. Hence, for the anticipated 10-year life span of $LiFePO_4$ battery, also indicated in [44], the initial cost estimate of 175000 EUR (battery + inverter cost) would have to be adjusted by additional 11400 EUR annually, finally reaching 289000 EUR at the end of expected 10-year battery calendar life.

Regarding the inverter operational requirements, the sustained active power delivery is mainly affected by the battery power rating and its respective discharge energy capacity [19]. On the other hand, the reactive output power Q_{ESS} is cycled between the AC grid and the sufficiently-sized DC link capacitor, whose capacitance C_{dc} needs to satisfy the following inequality condition [46]:

$$C_{dc} \geq \frac{S_{ESS,n}}{2\pi f_{grid} U_{dc} \Delta U_{dc}}. \tag{7}$$

where $S_{ESS,n}$ is the inverter apparent power rating, f_{grid} is the grid voltage frequency, U_{dc} is DC link average voltage (equal to battery terminal voltage), and ΔU_{dc} is the acceptable magnitude of DC link voltage ripple. Moreover, the DC link voltage magnitude U_{dc} which facilitates grid power delivery with minimum voltage distortion (under symmetric load conditions) is determined based on the following inequality condition with respect to voltage modulation index M [47]:

$$M = \frac{2U_{ph}}{U_{dc}} = \frac{2\sqrt{2}U_{L,rms}}{\sqrt{3}U_{dc}} \leq \frac{2}{\sqrt{3}} \tag{8}$$

where U_{ph} is the peak value of sinusoidal phase voltage reference, and $U_{L,rms}$ is the related line voltage RMS value. For the drilling rig microgrid line voltage RMS rating of 600 V (Section 2) the DC link voltage lower limit of 850 V is obtained herein. The above condition also determines the minimum required battery terminal voltage during discharging operation.

The battery system configuration in this work has been based on the 3.2V/100Ah $LiFePO_4$ battery cell [41]. Figure 9 shows the static characteristics of battery equivalent circuit parameters for a single $LiFePO_4$ battery cell with respect to cell state-of-charge:

$$\xi = \frac{q_b}{Q_b} = -\frac{1}{Q_b}\int i_b dt \,, \tag{9}$$

where Q_b is the battery charge capacity, and q_b is the accumulated battery charge.

The above characteristics have been recorded by means of suitable test setup in [48]. The experimentally-recorded open circuit voltage U_{oc} and equivalent internal resistance R_s (comprising ohmic resistance and steady-state polarization effects) have rather flat characteristics for a wide range of battery cell state-of-charge ξ, except for a deeply discharged and fully-charged cell, where more prominent state-of-charge variations are observed.

Assuming battery configuration as a series-connected string and also taking into account that cell idling terminal voltage u_{cell} would be larger than 3.2 V (Fig. 9) over the wide range of cell state-of-charge, the following inequality condition can be used to determine the number of battery cells N_{cell} required for the target battery storage capacity W_{st}:

$$N_{cell} \geq ceil\left(\frac{W_{st}}{Q_b u_{cell}}\right), \tag{10}$$

which yields $N_{cell} \geq 367$ cells for W_{st} = 117.5 kWh. Based on the chosen number of cells N_{cell} = 370 and the open-circuit voltage characteristic in Fig. 9, the maximum and minimum idling DC link voltage values are estimated to 1258 V and 1073 V, respectively. The latter result, being 25% larger than the minimum DC link voltage obtained according to (8), indicates that favorable quality of inverter AC output voltage modulation may be expected in practical applications.

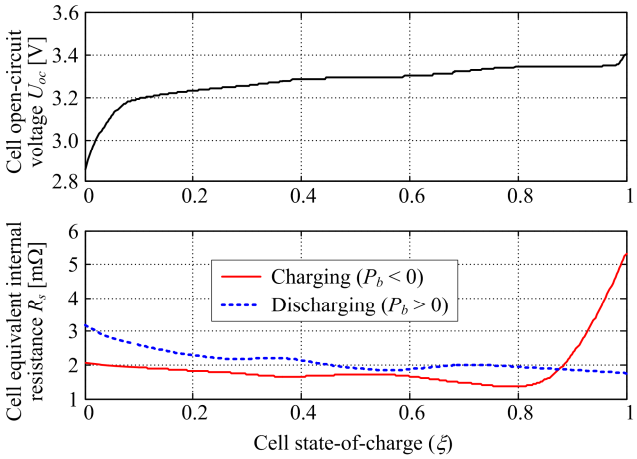

Figure 9. Recorded open-circuit voltage and total internal resistance static characteristics of chosen 3.2V/100 Ah $LiFePO_4$ battery cell within prospective battery energy storage system.

4. ESS-based microgrid energy management control system

This section outlines the proposed energy management control strategy for the drilling rig microgrid, which includes the generator scheduling and power flow distribution, and the charging/discharging control of the considered battery energy storage system, which have been included within the overall averaged microgrid simulation model aimed at analyzing the microgrid power flows.

4.1. Energy management control system outline

The principal block diagram of the considered drilling rig microgrid energy management system based on the battery energy storage system outlined in previous section is shown in Fig .10. The overall control strategy comprises the diesel generator power-plant rule-based control strategy for the purpose of determining the required number of generators based on averaged active and reactive power demands, supplied from the suitably tuned adaptive averaging filter (previous section). Based on the number of running generators and instantaneous active and reactive power demand (field data), the rule-based power-plant control strategy distributes the grid load between the active power-plant generators and the energy storage system.

Since battery energy storage system needs to be periodically charged from the grid, it needs to be equipped with a suitable state-of-charge controller which commands appropriate power demand to the grid converter. This charging command and battery state-of-charge also need to be made available to the rule-based control strategy, so that the power-plant would be able to provide the battery charging power in the case when battery state-of-charge becomes too low. Otherwise, the battery energy storage system might become over-discharged if frequent discharging requests are commanded, which would result in energy storage aging and cycle life reduction, as discussed in Section 3. Battery charging or discharging command is enabled by the superimposed-level rule-based control strategy and forwarded to the battery energy storage system power converter which facilitates the bidirectional active power flow with respect to battery system, along with supplying the drilling rig microgrid with required peak reactive power.

The dynamic equations within the simulation model in Fig. 10 (e.g. those corresponding to the battery energy storage system) are solved by using the fourth-order variable-step Runge-Kutta integration method, implemented within Matlab/Simulink environment with relative and absolute tolerances of 10^{-3} and 10^{-6}, respectively, which should result in favorable model precision. Since the time resolution of the simulation model inputs (microgrid active and reactive power requirements in Fig. 10) was predetermined by the field data collection system sampling period (T = 5 s), the model input data between sampling instants are linearly interpolated in time in order to provide for smooth simulation model inputs.

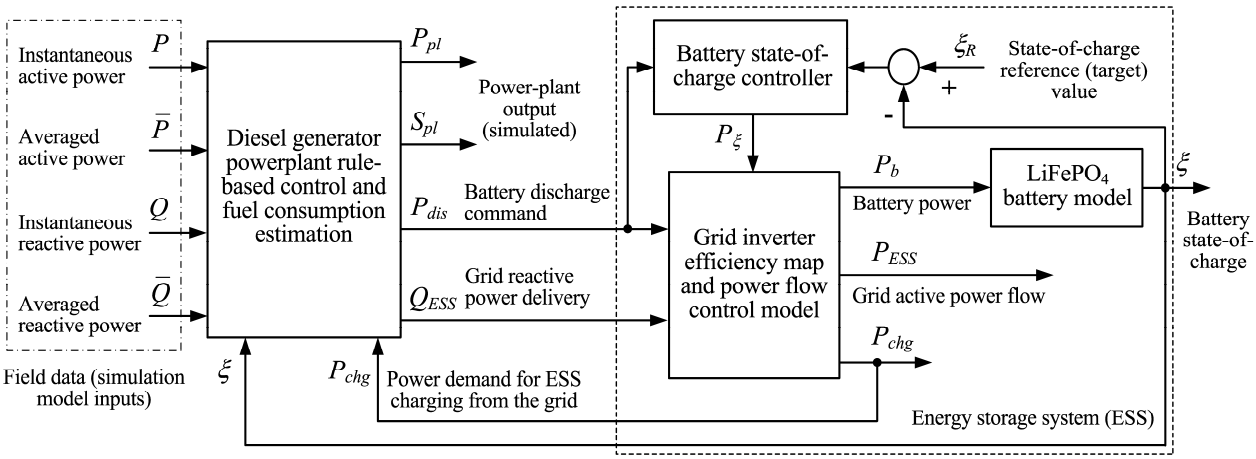

Figure 10. Principal block diagram of drilling rig AC microgrid energy management system simulation model.

4.2. Power-plant rule-based control scheme

Figure 11 shows the proposed superimposed rule-based control scheme comprising a generator scheduling control logic and straightforward power-plant generator demand management based on the requirement of even active and reactive load distribution between generators that are currently on-line (see Section 3). The control strategy may also be extended with the on-line open-loop estimation of the power-plant fuel consumption based on the generator fuel consumption map (Fig. 6) and power-plant active power monitoring.

The required number of power-plant generators is determined by using a switching logic based on the averaged grid apparent power demand calculated from the averaged active and reactive power demands (bottom portion of Fig. 11). Namely, the averaged apparent power is compared with the available apparent power from the number of generators N_{SG} currently in operation. If the generator upper switching threshold is reached or if the battery is currently operating at rather low state-of-charge levels (low ξ threshold), the number of required generators is incremented by one, thus ultimately increasing the power-plant output power needed for the grid power supply, and also facilitating timely battery recharging (see e.g. [17]), wherein a higher value of low-ξ threshold would correspond to a more conservative battery management, and vice versa. On the other hand, if the battery is close to fully-charged state or the power-plant averaged apparent power is rather low with respect to potentially available apparent power $N_{SG}S_N$ from the generators currently on-line, the number of generators is decreased by one. It should be noted that the generator turn on/turn off switching logic also incorporates a time delay in order to emulate realistic generator scheduling which requires generator starting up, bringing it up to grid-synchronous speed and finally connecting it to the grid. The same delay may also be used to emulate gradual generator disengagement. The parameters of the proposed generator scheduling switching logic are listed in Table 1.

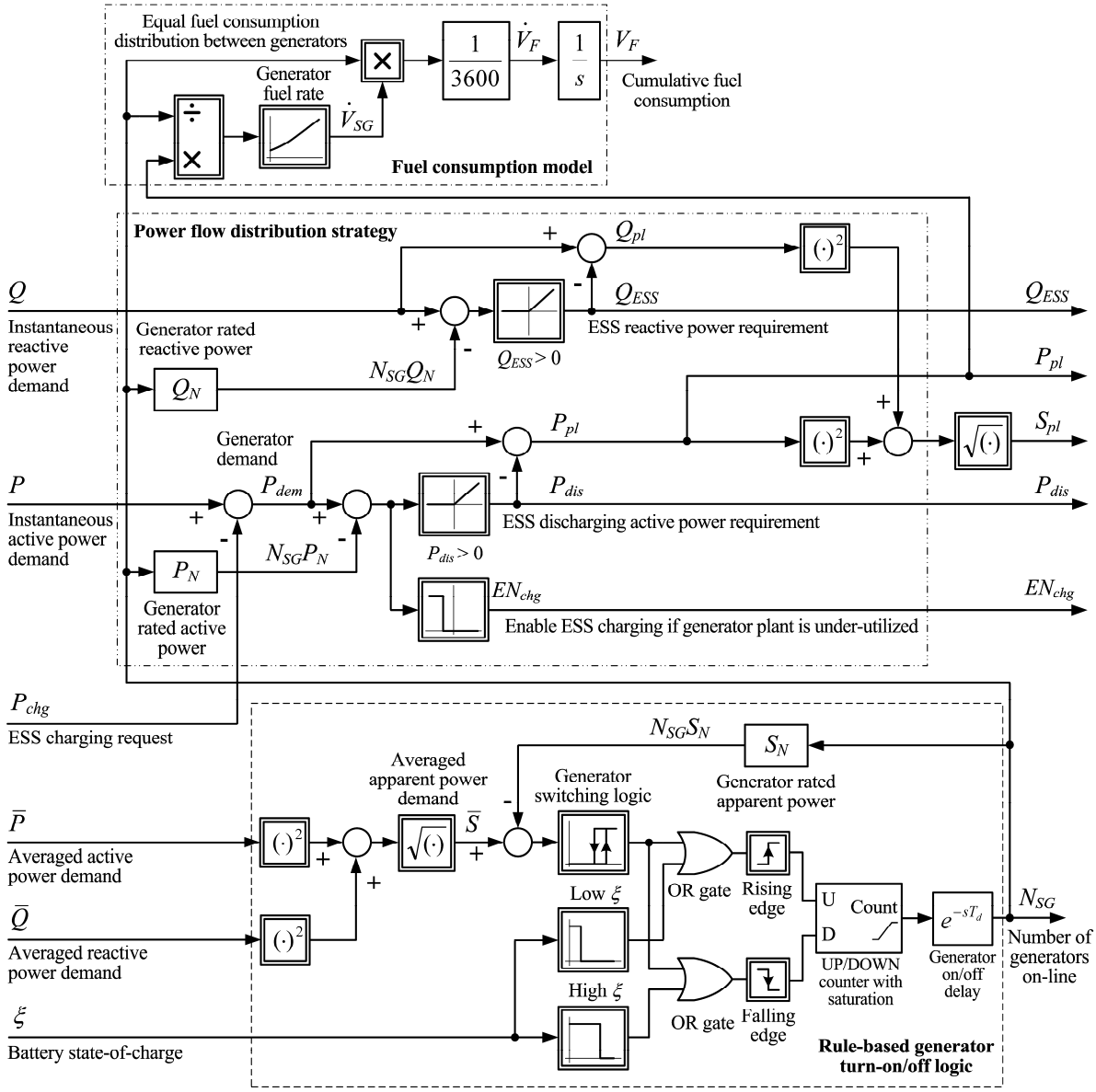

Figure 11. Block diagram of power-plant rule-based control strategy comprising generator turn-on/off logic with equal load distribution between active generators, and fuel consumption estimator based on generator fuel rate map.

The power-plant active and reactive instantaneous power distribution strategy (shown in middle portion of Fig. 11) is based on the requirement that generators currently on-line can be loaded up to their active and reactive power ratings (P_N and Q_N), with the additional condition that generator load should be distributed equally between currently active generators. This mandates that the total instantaneous active and apparent power-plant loads P_{pl} and Q_{pl} are limited to $N_{SG}P_N$ and $N_{SG}Q_N$, respectively, while the active and reactive power peak loads with respect to instantaneous power demands[‡] P and Q would be supplied by the battery energy storage system equipped with the grid-tied power converter (Fig. 8), and characterized by

[‡] In practical applications, instantaneous grid active and reactive power requirements could be provided within the framework of supervisory grid voltage and frequency droop control (see. e.g. [43]) in combination with instantaneous diesel power-plant output measurement.

fast response. Note that in the above power-plant active power demand P_{dem} calculation the anticipated instantaneous grid active load P would need to be augmented by the battery energy storage charging power demand P_{chg} (with negative battery power corresponding to charging case, see Fig. 8). In this way, battery charging request could be accommodated by the power-plant, provided that charging would be enabled (EN_{chg} flag in Fig. 11) based on the power-plant surplus active power availability (enabling logic block in Fig. 11).

Finally, the control strategy may also include on-line estimation of cumulative power-plant fuel consumption V_F (top of Fig. 11) based on the aforementioned condition of equal generator load distribution. In this way the open-loop fuel consumption estimation is further simplified because a single generator fuel consumption map can be used for the time-integration (accumulation) of power-plant fuel rate input $\dot{V}_F$ in simulations.

Table 1. Parameters of rule-based control strategy.

Parameter:	**Value:**
Generator switching logic turn-on threshold	$0.98S_N$
Generator switching logic turn-off threshold	$0.85S_N$
Battery charging enable threshold	$0.2P_N$
High ξ threshold	0.85
Low ξ threshold	0.65 (0.40)
Generator turn on/turn off delay T_d	3 minutes

4.3. Battery charging/discharging control system

Figure 12 represents the block diagram of the battery charging/discharging control system, which also includes the battery power flow-based dynamic model and power converter efficiency-based quasi-static model, also providing for the calculation of inverter line current RMS value I_L based on the well-known apparent power vs. line voltage and current relationship ($S_{ESS} = \sqrt{3}U_L I_L$) under "stiff" grid line voltage U_L conditions. As indicated in Figs. 10 and 11, battery discharging command ($P_{dis} > 0$) is forwarded from the superimposed power-plant rule-based energy management control system, which also automatically disables the battery charging controller during discharging power demands (EN_{chg} flag is OFF in that case). Battery charging control is based on the proportional (P) type controller which commands appropriate charging power demand ($P_\xi < 0$), limited below the battery rated charging power (P_{sat} = 80 kW herein). The state-of-charge P controller tuning has been aimed towards achieving a fast and well-damped closed-loop response, with the tuning procedure outlined in Appendix B.

For the purpose of simplicity, the energy storage system grid-tied converter has been modeled by using power converter efficiency static characteristic shown in Fig. 13. The efficiency characteristic $\eta_{grid}(S_{ESS})$ has been presented in the form of an efficiency map, as illustrated in [49]. The efficiency vs. apparent power map used herein is based on the results presented in [50], and extended to cover for the anticipated energy storage system apparent power range (ΔS = 0.6 MVA). The grid converter apparent power S_{ESS} has been used as efficiency curve input parameter because it effectively determines power converter switching and conduction losses [51], and would thus also be able to accommodate for grid filter ohmic losses. Finally, the power converter model may also include the small power converter lag T_L due to inner current control loop dynamics in order to account for realistic inverter output power transient effects.

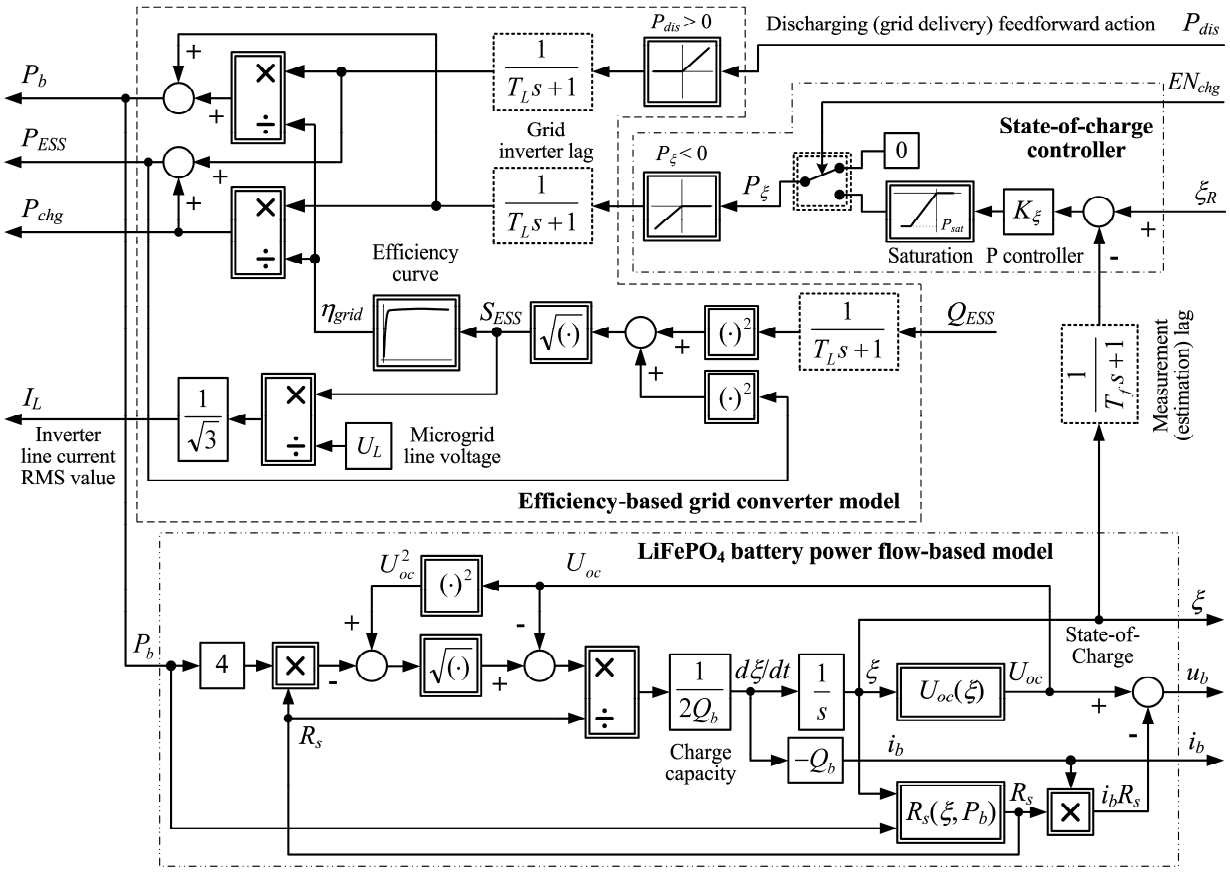

Figure 12. Block diagram representation of energy storage system charging/discharging control strategy, including grid inverter efficiency and line current RMS model, proportional-type state-of-charge controller and nonlinear power flow-based battery model.

The battery power flow model in Fig. 12 is based on the battery state-of-charge definition (10) and battery output power equation $P_b = u_b i_b = U_{oc} i_b - i_b^2 R_s$ (Fig. 8), which are used to build the following straightforward battery power flow-based model [16] suitable for prospective energy storage system simulation studies:

$$\frac{d\xi}{dt} = f(\xi, P_b) = \frac{\sqrt{U_{oc}^2(\xi) - 4R_s(\xi, P_b)P_b} - U_{oc}(\xi)}{2R_s(\xi, P_b)Q_b}. \quad (11)$$

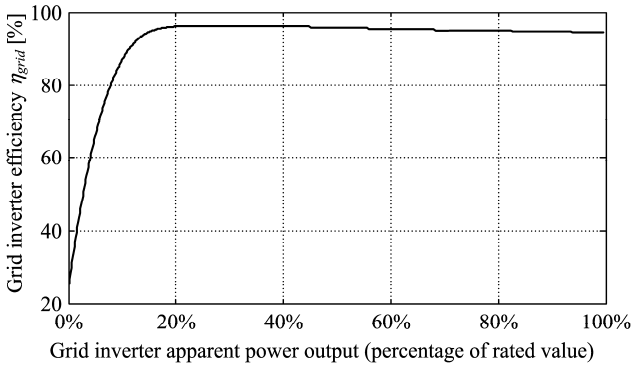

Figure 13. Grid inverter efficiency curve used in simulation analysis.

5. Energy management strategy simulation results and cost-benefit analysis

The power-plant energy management control strategy presented in Section 4 has been tested by means of simulations based on the grid load profiles from Section 3, for two distinct state-of-charge threshold settings related to battery recharging from the grid (Section 4). Based on fuel expenditure reduction capabilities of the proposed energy management system, the potentials for carbon-dioxide emissions reduction are estimated and battery ESS return-of-investment period is assessed.

5.1. Simulation results

The drilling rig AC microgrid power flow simulations have been carried out based on the simplified averaged power flow model whose overall layout and principal components have been described in Section 4, and illustrated by Figs. 10 – 13. The high-frequency phenomena and microgrid voltage/current total harmonic distortion (THD), which are related to inverter switching operation, have not been analyzed herein, because a simplified inverter model based on efficiency maps and equivalent current control loop lag behavior has been used to facilitate simple and straightforward power-flow analysis.

Figure 14 shows the results for the case of rather high low ξ threshold setting (0.65) from Table 1, which tends to bring additional generators on-line even when battery is only moderately discharged (battery-conserving energy management strategy). For this particular scenario, the energy management control strategy results in the ESS apparent power values within the considered grid inverter power ratings ($S_{ESS} \leq 0.6$ MVA), with grid active power delivery from the battery of up to 0.4 MW (top plots in Fig. 14). The considered battery-conserving energy management strategy also produces 78 generator turn-on/turn-off switching events, which is roughly 2.6 times more than in the "ideal" (load preview) case analyzed in Section 3. This increase in generator requirements is primarily due to additional requests for battery recharging when low state-of-charge is indicated (Fig. 11) and realistic energy storage system losses.

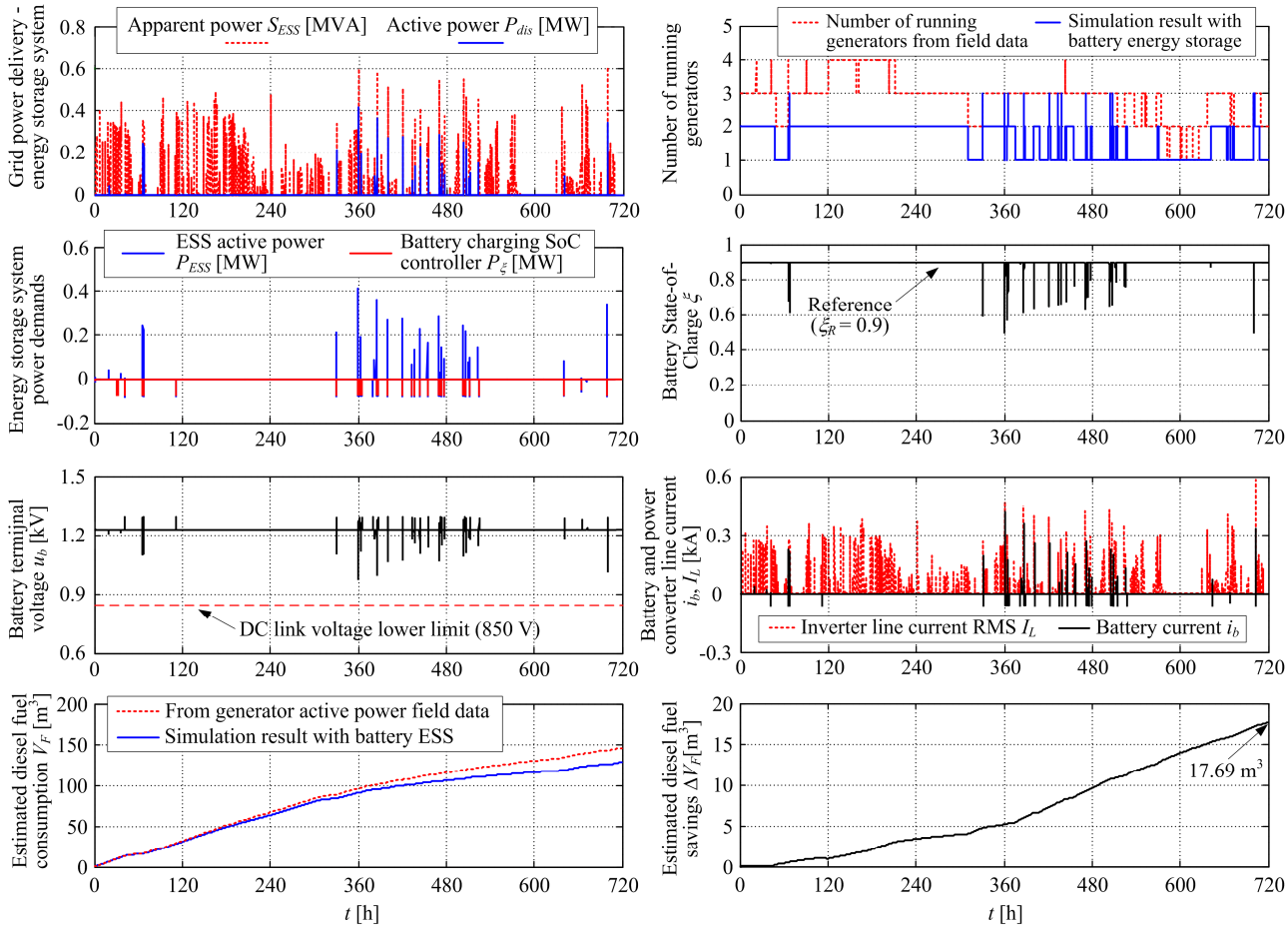

Figure 14. Grid inverter power delivery and comparative number of running generators, battery charging/discharging power demands, state-of-charge, terminal voltage and current rates, and fuel consumption results for battery-conserving energy management strategy.

The middle plots in Fig. 14 indicate that the considered battery ESS is characterized by relatively small state-of-charge excursions from the target value ξ_R = 0.9 (chosen herein to avoid overcharging and associated aging issues [45]), which is commanded to the proposed state-of-charge controller and maintained during battery idling intervals. The superimposed energy management strategy, which provides the battery discharging command, also effectively prevents the battery state-of-charge from dropping below 0.5. This is facilitated by aforementioned timely bringing of additional generators on-line for the purpose of battery recharging, which is beneficial from the standpoint of battery cycle life (see discussion in Section 3). The battery terminal voltage and current plots in Fig. 14 indicate that by using this strategy: (i) power converter DC link voltage would be kept above the minimum required value of 850 V for correct operation (Section 4), and (ii) the discharging current is within the acceptable load envelope for the particular battery, which can accommodate up to 400 A during discharging [41]. As expected, the inverter line current RMS requirement is predominantly due to the additional microgrid reactive power requirement, commanded by the superimposed rule-based control strategy (cf. top left plot in Fig. 14). Finally, the power-plant estimated fuel consumption under the proposed energy management control strategy is compared to

the result obtained from generator field data (bottom plots in Fig. 14), which indicates there is a clear potential for fuel consumption reduction. Namely, fuel savings with respect to power-plant operation in the field are estimated to $\Delta V_F = 17.69$ m^3 over the 30-day period. This corresponds to a 12.07% estimated fuel efficiency improvement for the particular simulation scenario including the proposed energy management strategy and battery ESS.

Simulation results for the case of battery-intensive energy management strategy (with low-ξ threshold equal to 0.4) are shown in Fig. 15. These results indicate that the peak apparent and active power delivery from the energy storage system may reach 0.8 MVA and 0.6 MW, respectively for the particular simulation scenario. This is primarily due to reduced requirement for bringing additional generators on-line related to aforementioned deeper battery discharge allowance, wherein the number of generator turn-on/turn-off events has been reduced to 66 (a 15% decrease compared to battery-conservative strategy). The aforementioned battery-intensive strategy naturally results in deeper energy storage discharging, and larger state-of-charge and grid inverter DC voltage fluctuations, with state-of-charge and DC link voltage dropping to 0.2 (20%) and 600 V, respectively in the extreme case observed in Fig. 15. Moreover, this strategy may also result in battery current overload (i.e. the 1 kA peak battery current is observed in this scenario), which may mandate battery system shutdown in order to prevent thermal damage. This reliance on the battery for prolonged grid active power delivery and related reduction of additional generator engagement has yielded a minor improvement in fuel efficiency when compared to battery-conservative strategy (0.21 m^3 less fuel expended). However, the aforementioned 12.22% overall fuel efficiency improvement with respect to field data might not justify such "harsh" battery operating regimes which may shorten the battery life [40], especially when battery replacement costs are taken into account (see Section 4).

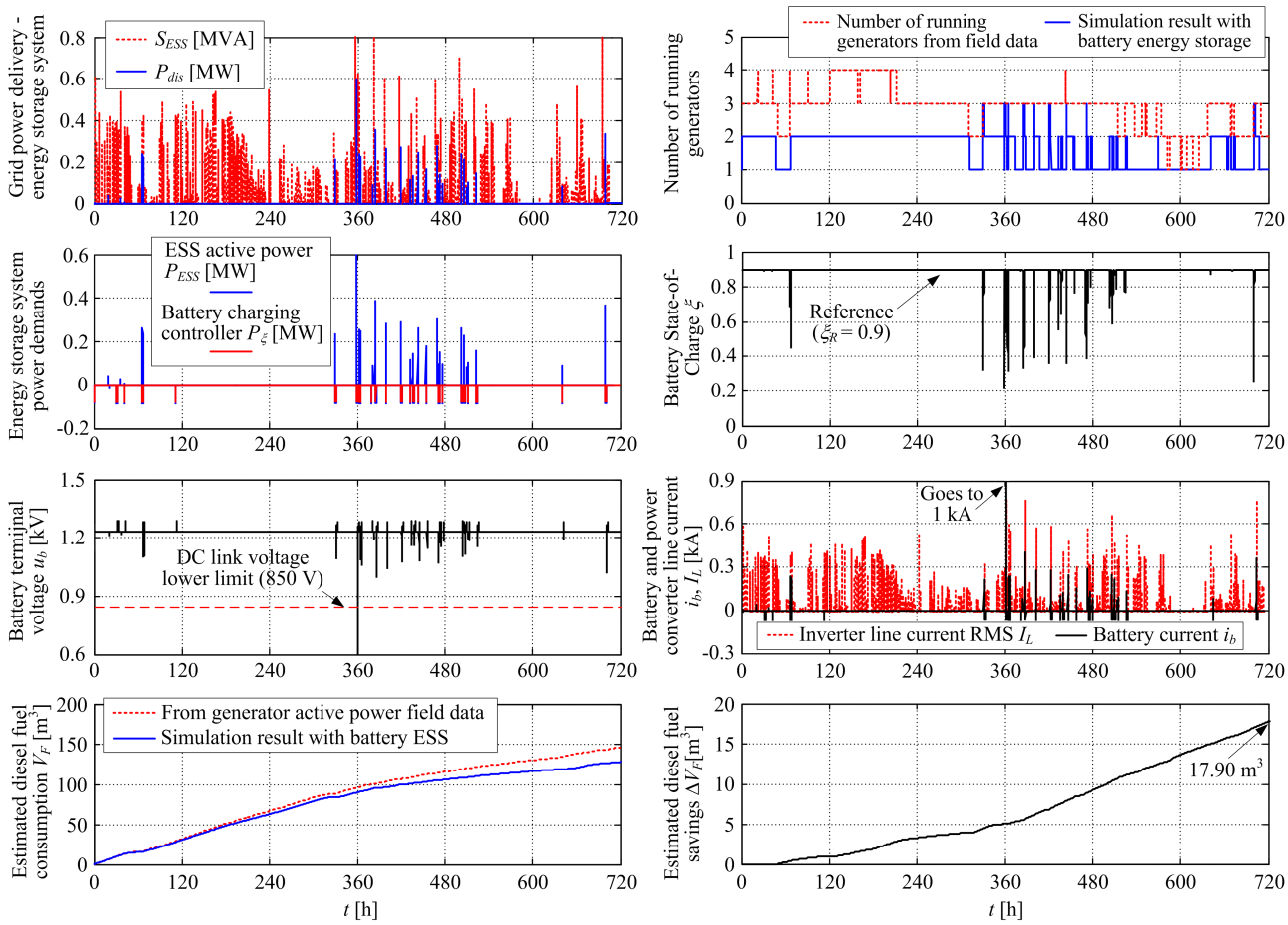

Figure 15. Grid inverter power delivery and comparative number of running generators, battery charging/discharging power demands, state-of-charge, terminal voltage and current rates, and fuel consumption results for battery-intensive energy management strategy.

5.2. Assessment of financial gains and CO_2 emissions reduction potentials

The aforementioned simulated diesel fuel savings are used to estimate the possible return-of-investment period of the added battery energy storage system, and are also correlated with the corresponding carbon-dioxide (CO_2) emissions reductions. Since similar fuel expenditure results have been obtained for the two distinct energy management strategies analyzed above, battery-conservative strategy result is used in the assessment because this strategy is much less likely to incur additional battery replacement costs (when compared to battery-intensive ESS operation).

The financial gain of ESS operation and related return-of investment period have been estimated based on the wholesale diesel fuel price for Croatia, which is estimated to 900 EUR/m^3 by excluding the 25% VAT rate billed to the drilling contractor from the retail diesel fuel price obtained from [52]. Based on this, the cost savings associated with fuel expenditure reduction of 17.69 m^3 over the observed 30-day period would amount to 15921 EUR. Furthermore, assuming continuous power-plant operation under similar load conditions, the projected ESS return-of-investment period ΔT_R (expressed in days of continuous operation) could be estimated based on ESS capital cost (175000 EUR) and operation and

maintenance annual costs (11400 EUR/year). The following simple expression could be used to obtain such a rough estimate of return-of-investment period:

$$d \cdot \Delta T_R \cdot 900\left[\frac{\text{EUR}}{\text{m}^3}\right] \cdot \frac{\Delta V_F(30\,\text{days})}{30\,\text{days}} = 175000\,\text{EUR} + 11400\left[\frac{\text{EUR}}{\text{year}}\right] \cdot ceil\left(\frac{\Delta T_R}{365}\right), \tag{12}$$

where d is the power-plant duty ratio related to scheduled downtime due to maintenance and site-to-site transportation, while the operation and maintenance costs (11400 EUR/year) are included as annual fixed costs (modeled by rounding towards the ceiling value).

By iteratively solving the above equation, the ideal ESS return-of-investment period ΔT_R is estimated to 352 days of continuous ESS operation ($d = 1$) under the assumption of similar drilling rig operating conditions. The return-of-investment periods obtained for different duty ratio values are given in Table 2. The results show that even in the case of 50% duty ratio, profitable operation should be reached within approximately 26 months, which is still nearly five times shorter than the anticipated battery system calendar life (10 years).

Table 2. Battery ESS return-of-investment periods with respect to power-plant utilization (duty ratio).

Power-plant duty ratio d	0.9	0.8	0.7	0.6	0.5
Return-of-investment period ΔT_R [days]	414	466	533	621	788

It should be noted, however, that the above analysis did not include the influence of reduced generator utilization in terms of shorter cumulative time of operation. Namely, this might provide additional benefits in terms of diesel generator life extension due to reduced mechanical component wear, and related reduction in power-plant diesel generator maintenance and periodic overhaul costs.

Finally, the drilling rig environmental impact improvement based on ESS utilization is assessed herein in terms of projected CO_2 emissions reduction. For that purpose, a straightforward proportional relationship is used to determine the mass of carbon-dioxide m_{CO2} released into the atmosphere based on the diesel fuel expenditure V_F [53]:

$$m_{CO2}[\text{t}] = 2.65 \cdot V_F[\text{m}^3], \tag{13}$$

which yields the estimated emission reduction of 46.88 tons of CO_2 for the estimated fuel expenditure reduction $\Delta V_F = 17.69$ m^3 due to utilization of battery ESS and energy management strategy during the observed 30-day period.

Under the near-idealistic assumption of battery ESS operation with duty ratio $d = 0.9$, and utilization of the proposed ESS-based energy management strategy under similar microgrid load conditions, simple linear extrapolation may yield the theoretical CO_2 emission reduction upper bound of approximately 5130 t over the anticipated 10-year battery system lifetime. Naturally, accuracy of the above rather coarse CO_2 emission estimates may be further improved by using a more

comprehensive diesel engine combustion-based emission model [54]. For the non-ideal combustion case the emission model may also incorporate partial combustion-related formation of carbon-monoxide, as shown in [55]. However, that is beyond the scope of this work.

6. Conclusion

The paper has presented the design of an energy management strategy for the oil drilling rig AC microgrid supplied from a diesel-engine power-plant. The strategy included the averaged microgrid load-based generator scheduling strategy and a power-plant active/reactive power flow control, and the peak shaving control system based on a suitably chosen battery energy storage system (ESS) equipped with appropriate charging/discharging controller. The energy management system design has been based on insights obtained by analyzing the drilling rig microgrid power flow field data, recorded over a 30-day period of drilling-intensive operations. These results indicated a clear potential for the reduction of number of generators supporting the microgrid, provided that peak loads would be covered from the suitably-sized energy storage system. A lithium-iron-phosphate ($LiFePO_4$) battery energy storage system equipped with appropriately sized grid-tied inverter has been parameterized for the required energy storage capacity and apparent grid power delivery, and overall battery ESS investment and operation/maintenance costs have been estimated based on available literature.

The effectiveness of the proposed energy management control strategy has been verified by means of simulations utilizing realistic drilling rig microgrid power profiles based on field data as simulation inputs, and it has also been compared with power-plant management practices currently implemented in the field. The comparative results have indicated a clear fuel efficiency improvement potential of the hybrid (ESS-based) power-plant energy management control strategy, amounting to 12% fuel expenditure reduction compared to the conventionally operated power-plant. The battery ESS return-of-investment period has been estimated to between one and two years depending on the power-plant utilization (duty ratio), which, in the latter case, represents 20% of the anticipated battery ESS calendar life. Based on the aforementioned fuels savings estimates, a notable CO_2 emissions reduction potential has also been identified, with projected cutback of CO_2 atmospheric release possibly reaching 5000 t for a single land-based drilling rig over the anticipated battery ESS useful service life.

Future work is going to be aimed towards collecting and analyzing of a more comprehensive drilling rig microgrid data set covering the whole span of drilling rig operation from the start of the drilling process to well completion, and comprehensive statistical analysis of thus obtained data. The additional experimental data may then be used as a basis for a more comprehensive assessment of energy storage system requirements, as well as implementation of different off-line optimization procedures aimed at diesel power-plant fuel efficiency improvement, and related developments of real-time optimal control strategies for such a hybridized drilling rig microgrid and their comparison to rule-based control.

Acknowledgement

This work has been supported by the Croatian Science Foundation (HRZZ) through the "Optimization of renewable electricity generation systems connected in a microgrid" collaborative project, grant No. 08/40, and also by the University of Zagreb through the research project "Energy management control of drilling rig microgrid", grant No. 2013-ZUID-2/5.5.2.8. Technical support related to the development of data acquisition software for oil-field data collection provided by Anton Lisac, dipl. ing. and Zdravko Kučan, ing. from Nev-El Ltd. is also highly appreciated, as well as the organizational support provided by Josip Mišković, dipl. ing. from CROSCO – Integrated Drilling & Well Services. Useful discussions with Zvonimir Popić, mag. ing. from INA d.d. regarding power flow analysis and battery energy storage system parameterization have also been appreciated, as well as the assistance of Ante Komljenović, mag. ing from the Faculty of Mechanical Engineering and Naval Architecture, University of Zagreb, during the field data pre-processing stage. The continued support of oil drilling systems research activities provided by HELB Ltd. is also gratefully acknowledged herein. Finally, authors would also like to express their appreciation of the efforts of the Associate Editor and anonymous reviewers whose comments and suggestions have helped to improve the quality of the presented subject matter.

References

[1] S. Sorrell, J. Speirs, R. Bentley, A. Brandt, and R. Miller: "Global oil depletion: A review of the evidence", Energy Policy, Vol. 38, No. 9, 5290 – 5295, 2010.

[2] U. Bardi: "Peak Oil: The four stages of a new idea", Energy, Vol. 34, No. 3, pp. 323 – 326, 2009.

[3] Statoil, A.S.A.: "Statoil 2014 Sustainability report" (http://www.statoil.com/sustainability), Norway, 2015.

[4] British Petroleum PLC: "BP Sustainability Report 2014" (http://www.bp.com/sustainability), UK, 2015.

[5] C. Bylin, Z. Schaffer, V. Goel, D. Robinson, A. N. Campos, and F. Borensztein: "Designing the Ideal Offshore Platform Methane Mitigation Strategy", Proceedings of SPE International Conference on Health, Safety and Environment in Oil and Gas Exploration and Production, SPE paper No. 126964, Rio de Janeiro, Brazil, 2010.

[6] D. Luo and X. Zhao: "Modeling the operating costs for petroleum exploration and development projects", Energy, Vol. 40, No. 1, pp. 189 – 195, 2012.

[7] M. J. Mazzetti, P. Nekså, H. T. Walnum, and A. K. T. Hemmingsen: "Energy-Efficient Technologies for Reduction of Offshore CO_2 Emmissions", SPE Oil and Gas Facilities, Vol. 3, No. 1, pp. 89 – 96 (SPE paper No. 169811), 2014.

[8] Baker-Hughes: "International Rig Counts" (http://phx.corporate-ir.net/phoenix.zhtml?c=79687&p=irol-rigcountsintl), November 2015.

[9] W. C. Lyons and G. J. Plisga (ed.): "Standard Handbook of Petroleum & Natural Gas Engineering", 2nd ed., Gulf Professional Publishing (imprint of Elsevier), Burlington, MA, USA, 2005.

[10] P. P. A. Caldeira and E. H. Watanabe: "Compensation of Power Factor in Rectifier Systems Utilized in Oil Drilling Rigs", IEEE Transactions on Industry Applications, Vol. 24, No. 2, pp. 301 – 307, 1988.

[11] M. J. Kaiser and B. F. Snyder: "The Offshore Drilling Industry and Rig Construction in the Gulf of Mexico", Chapter 2, Lecture Notes in Energy 8, Springer-Verlag, London, 2013.

[12] M. Kanoğlu, S. K. Işık, and A. Abuşoğlu: "Performance characteristics of a Diesel engine power plant", Energy Conversion and Management, Vol. 46, No. 11-12, pp. 1692 – 1702, 2005.

[13] G. Hunt and J. Szymborsky: "Achievements of an ABSOLYTE Valve-Regulated Lead-Acid Battery Operating in a Utility Battery Energy Storage System (BESS) for 12 years", EESAT 2009 Biennial International Conference, Seattle, WA, 2009.

[14] P. Yadav, R. Kumar, S. K. Panda, and C.S. Chang: "An Improved Harmony Search algorithm for optimal scheduling of the diesel generators in oil rig platforms", Energy Conversion and Management, Vol. 52, No. 2, pp. 893 – 902, 2011.

[15] S. Koohi-Kamali, N. A. Rahim, and H. Mokhlis: "Smart power management algorithm in microgrid consisting of photovoltaic, diesel, and battery storage plants considering variations in sunlight, temperature, and load", Energy Conversion and Management, Vol. 84, pp. 562–582, 2014.

[16] N. Kim, S. W. Cha, and H. Peng: "Optimal Equivalent Fuel Consumption for Hybrid Electric Vehicles", IEEE Transactions on Control Systems Technology, Vol. 20, No. 3, pp. 817 – 825, 2012.

[17] M. Cipek, D. Pavković, and J. Petrić: "A control-oriented simulation model of a power-split hybrid electric vehicle", Applied Energy, Vol. 101, pp. 121-133, 2013.

[18] S. Rehman, I. M. El-Amin, F. Ahmad, S. M. Shaahid, A. M. Al-Shehri, J. M. Bakhashwain, and A. Shash: "Feasibility study of hybrid retrofits to an isolated off-grid diesel power plant", Renewable and Sustainable Energy Reviews, Vol. 11, No. 4, pp. 635 – 653, 2007.

[19] L. K. Gan, J. K. H. Shek, and M. A. Mueller: "Hybrid wind–photovoltaic–diesel–battery system sizing tool development using empirical approach, life-cycle cost and performance analysis: A case study in Scotland", Energy Conversion and Management, Vol. 106, pp. 479 – 494, 2015.

[20] J.-Y. Kim, J.-H. Jeon, S.-K. Kim, C. Cho, J. H. Park, H.-M. Kim, and K.-Y. Nam: "Cooperative Control Strategy of Energy Storage System and Microsources for Stabilizing the Microgrid during Islanded Operation", IEEE Transactions on Power Electronics, Vol. 25, No. 12, pp. 3037 – 3048, 2010.

[21] A. Etxeberria, I. Veichu, H. Camblong, and J.-M. Vinassa: "Comparison of three topologies of a hybrid energy storage system for microgrids", Energy Conversion and Management, Vol. 54, No. 1, pp. 113 – 121, 2012.

[22] J. K. Kaldellis, D. Zafirakis, K. Kavadias: "Techno-economic comparison of energy storage systems for island autonomous electrical networks", Renewable and Sustainable Energy Reviews, Vol. 13, No. 2, pp. 378 – 392, 2009.

[23] V. Fernão-Pires, E. Romero-Cadaval, D. Vinnikov, I. Roasto, and J. F. Martins: "Power converter interfaces for electrochemical energy storage systems – A review", Energy Conversion and Management, Vol. 86, pp. 453 – 475, 2014.

[24] F. Guarino, P. Cassarà, S. Longo, M. Cellura, E. Ferro: "Load match optimisation of a residential building case study: A cross-entropy based electricity storage sizing algorithm", Applied Energy, Vol. 154, pp. 380 – 391, 2015.

[25] J. K. Kaldellis: "Optimum autonomous wind-power system sizing for remote consumers, using long-term wind speed data", Applied Energy, Vol. 71, No. 3, pp 215 – 233, 2002.

[26] D. Pavković, M. Hoić, J. Deur, and J. Petrić: "Energy Storage Systems Sizing Study for a High-Altitude Wind Energy Application", Energy, Vol. 76, pp. 91 – 103, 2014.

[27] M. Cresta, F. M. Gatta, A. Geri, M. Maccioni, A. Mantineo, and M. Paulucci: "Optimal operation of a low-voltage distribution network with renewable distributed generation by NaS battery and demand response strategy: a case study in a trial site", IET Renewable Energy Generation, Vol. 9, No. 6, pp 549 – 556, 2015.

[28] A. Poullikkas: "A comparative overview of large-scale battery systems for electricity storage", Renewable and Sustainable Energy Reviews, Vol. 27, pp. 778 – 788, 2013.

[29] D. U. Sauer and H. Wenzl: "Comparison of Different Approaches for Lifetime Prediction of Electrochemical Systems – using Lead-Acid Batteries as Example", Journal of Power Sources, Vol. 178, No. 2, pp. 531 – 546, 2008.

[30] M. C. Díaz-de-Baldasano, F. J. Mateos, L. R. Núñez-Rivas, and T. J. Leo: "Conceptual design of offshore platform supply vessel based on hybrid diesel generator-fuel cell power plant", Applied Energy, Vol. 116, pp. 91 – 100, 2014.

[31] C. Craig, and M. Islam: "Integrated Power System Design for Offshore Energy Vessels and Deepwater Drilling Rigs", IEEE Transactions on Industry Applications, Vol. 48, No. 4, pp. 1251 – 1257, 2012.

[32] A. Dekka, A. R. Beig, S. Kanukollu, and M. S. Al Rahis: "Retrofitting of Harmonic Power Filters in Onshore Oil Drilling Rigs: Challenges and Solutions", IEEE Transactions on Industry Applications, Vol. 50, No. 1, pp. 142 – 154, 2014.

[33] Z. Lujun: "An energy-saving oil drilling rig for recovering potential energy and decreasing motor power", Energy Conversion and Management, Vol. 52, No. 1, pp. 359 – 365, 2011.

[34] Caterpillar Tractor Co.: "Caterpillar D399 Marine Generator Set" (https://marine.cat.com/cat-D399), 2015.

[35] D. Pavković, J. Deur, and A. Lisac: "A Torque Estimator-based Control Strategy for Oil-Well Drill-string Torsional Vibrations Active Damping Including an Auto-tuning Algorithm", Control Engineering Practice, Vol. 19, No. 8, pp. 836-850, 2011.

[36] P. C. Sen, and S. R. Doradla: "Symmetrical and Extinction Angle Control of Solid-State Series Motor Drive", IEEE Transactions on Industrial Electronics and Control Instrumentation, Vol. 23, No. 1, pp. 31 – 38, 1976.

[37] F. Gustafsson: "Adaptive Filtering and Change Detection", John Wiley and Sons Ltd., Chichester, UK, 2001.

[38] F. Katiraei and C. Abbey: “Diesel Plant Sizing and Performance Analysis of a Remote Wind-Diesel Microgrid”, Proceedings of the IEEE Power and Energy Society 2007 General Meeting, 8 pages, Tampa, FL, USA, 2007.

[39] International Renewable Energy Agency (IRENA): “Road Transport: The Cost of Renewable Solutions”, IRENA’s Costing Study (http://www.irena.org/publications), 2013.

[40] N. Omar, M. A. Monem, Y. Firouz, J. Salmien, J. Smekens, O. Hagazy, H. Gaulous, G.. Mulder, P. Van den Bossche, T. Coosemans, and J. Van Mierlo: “Lithium Iron Phosphate Based Battery – Assessment of Aging Parameters and Development of Life Cycle Model”, Applied Energy, Vol. 113, pp. 1575 – 1585, 2014.

[41] GWL/Power Group: “SE100AHA Cell Specification”, http://www.ev-power.eu, 2015.

[42] P. Arboleya, D. Diaz, J. M. Guerrero, P. Garcia, F. Briz, C. Gonzalez-Moran, J. Gomez Aleixandre: “An improved control scheme based in droop characteristic for microgrid converters”, Electric Power Systems Research, Vol. 80, No. 10, pp. 1215 – 1221, 2010.

[43] Q.-C. Zhong, and T. Hornik: “Control of Power Inverters in Renewable Energy and Smart Grid Integration”, John Wiley & Sons Ltd / IEEE Press, NY, USA, 2013.

[44] B. Battke, T. S. Schmidt, D. Grosspietsch, and V. H. Hoffmann: “A review and probabilistic model of lifecycle costs of stationary batteries in multiple applications”, Renewable and Sustainable Energy Reviews, Vol. 25, pp. 240 – 250, 2013.

[45] H. Rahimi-Eichi, U. Ojha, F. Baronti, and M.-Y. Chow: “Battery Management System – An Overview of Its Application in the Smart Grid and Electric Vehicles”, IEEE Industrial Electronics Magazine, Vol. 7, No. 2, pp. 5 – 16, 2013.

[46] G. V. Gohil, H. Wang, M. Liserre, T. Kerekes, R. Teodorescu, and F. Blaabjerg: “Reduction of DC-link Capacitor in Case of Cascade Multilevel Converters by means of Reactive Power Control”, Proceedings of the 29th Annual IEEE Applied Power Electronics Conference and Exposition (APEC 2014), pp. 231 – 238, 2014.

[47] J. W. Kolar and S. D. Round: “Analytical calculation of the RMS current stress on the DC-link capacitor of voltage-PWM converter systems”, IEE Proceedings – Electric Power Applications, Vol. 153, No. 4, pp. 535 – 543, 2006.

[48] D. Pavković, A. Komljenović, M. Hrgetić, and M. Krznar: “Experimental Characterization and Development of a SoC/SoH Estimator for a $LiFePO_4$ Battery Cell”, Proceedings of IEEE EUROCON 2015, pp. 397-402, Salamanca, Spain, 2015.

[49] H. Bindner, C. Ekman, O. Gehrke, and F. Islefsson: “Characterization of Vanadium Flow Battery”, Technical report Risø-R-1753(EN), Risø National Laboratory for Sustainable Energy, Roskilde, Denmark, 2010.

[50] M. Braun: “Reactive Power Supplied by PV Inverters – Cost-Benefit-Analysis”, Proceedings of 22nd European Photovoltaic Solar Energy Conference and Exhibition, 7 pages, Milan, Italy, 2007.

[51] S. S. Williamson, A. Emadi, and K. Rajashekara: "Comprehensive Efficiency Modeling of Electric Traction Motor Drives for Hybrid Electric Vehicle Propulsion Applications", IEEE Transactions on Vehicular Technology, Vol. 56, No. 4, pp. 1561 – 1572, 2007.

[52] European Commission: "Weekly Oil Bulletin: Consumer prices of petroleum products", (http://ec.europa.eu/energy/), November, 2015.

[53] I. J. M. Besselink, P. F. van Oorschot, E. Meinders and H. Nijmeijer: "Design of an efficient, low weight battery electric vehicle based on VW Lupo 3L", Proceedings of the 25th World Battery, Hybrid and Fuel Cell Electric Vehicle Symposium & Exhibition (EVS 25), 10 pages, Shenzen, China, 2010.

[54] J. Asprion, O. Chinellato, and L. Guzzella: "Optimisation-oriented modelling of the NO_x emissions of a Diesel engine", Energy Conversion and Management, Vol. 75, pp. 61 – 73, 2013.

[55] L. Lešnik, J. Iljaž, A. Hribernik, and B. Kegl: "Numerical and experimental study of combustion, performance and emission characteristics of a heavy-duty DI diesel engine running on diesel, biodiesel and their blends", Energy Conversion and Management, Vol. 81, pp. 534 – 546, 2014.

[56] D. Pavković, J. Deur, and I. Kolmanovsky, "Adaptive Kalman Filter-Based Load Torque Compensator for Improved SI Engine Idle Speed Control", IEEE Transactions on Control Systems Technology, Vol. 17, No. 1, pp. 98 – 110, 2009.

[57] R. Isermann, "Digital Control Systems", Vol. 1, Springer-Verlag, Berlin, 1989.

Appendix A: Adaptive Kalman filter for real-time field data averaging

The design of adaptive Kalman filter for the purpose of real-time power data averaging is based on the following stochastic second-order random-walk model [37] of power data variations, given in the following state-space form:

$$\begin{aligned} \mathbf{x}(k) &= \mathbf{F}\mathbf{x}(k-1) + \mathbf{\Omega}\boldsymbol{\nu}(k-1), \\ y(k) &= \mathbf{H}\mathbf{x}(k) + e(k), \end{aligned} \tag{14}$$

with the state vector defined as $\mathbf{x} = \begin{bmatrix} x & \dot{x} \end{bmatrix}^T$ (and x corresponding to active, reactive or apparent power estimates), $\boldsymbol{\nu} = [\nu_x \;\; \nu_{xd}]^T$ and e being the anticipated variances of stochastic state perturbations and measurement noise, respectively, and y being the model output (measurement), and system matrices **F**, **H** and **Ω** defined as follows (T is estimator sampling time):

$$\mathbf{F} = \begin{bmatrix} 1 & T \\ 0 & 1 \end{bmatrix}, \quad \mathbf{\Omega} = \begin{bmatrix} T & T^2/2 \\ 0 & T \end{bmatrix}, \quad \mathbf{H} = \begin{bmatrix} 1 & 0 \end{bmatrix}. \tag{15}$$

Since the stochastic state perturbations ν_x and ν_{xd}, and the measurement noise e are assumed to be mutually independent, the state perturbation covariance matrix **Q** and the noise variance r are also independent:

$$\mathbf{Q} = \begin{bmatrix} \mathrm{var}(\nu_x) & 0 \\ 0 & \mathrm{var}(\nu_{xd}) \end{bmatrix} = \begin{bmatrix} q_x & 0 \\ 0 & q_{xd} \end{bmatrix}, \quad r = \mathrm{var}(e), \tag{16}$$

where individual variance terms represent tuning parameters of the adaptive Kalman filter-based state estimator, whose block diagram is shown in Fig. 16. The proposed adaptive estimator incorporates the deterministic part of the state-space process model (14), and optimal gain calculation based on the anticipated properties of the stochastic perturbations within the model (so-called Ricatti matrix equations for gain vector update **K**) [37].

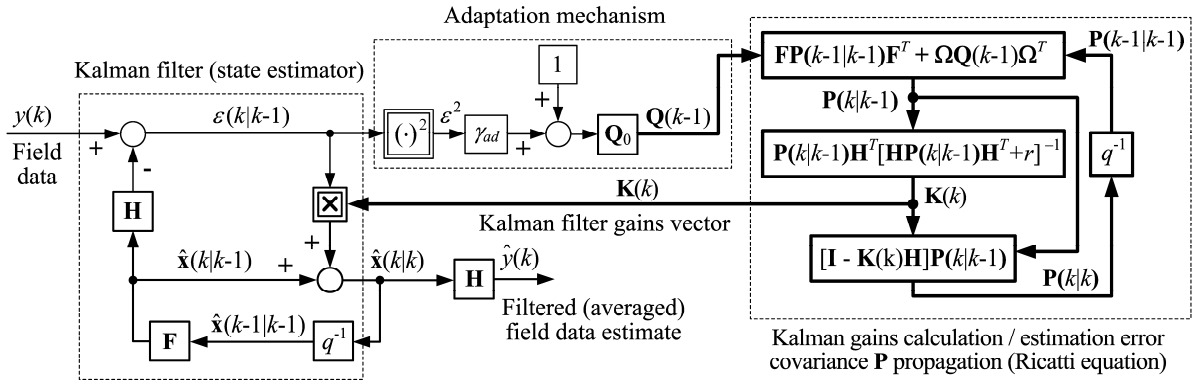

Figure 16. Block diagram representation of adaptive Kalman filter for power data averaging.

In order to facilitate fast estimator response in the case of large-magnitude power measurement variations, while maintaining favorable estimator noise suppression ability in the steady state (i.e. during low-magnitude power fluctuation intervals), the basic Kalman filter is augmented with an adaptation mechanism based on squared estimator prediction error:

$$\mathbf{Q} = \mathbf{Q}_0(1 + \gamma_{ad}\varepsilon^2), \tag{17}$$

where γ_{ad} is the squared prediction error weighting factor. In this way, coefficients of the state perturbation matrix **Q** are increased proportionally to prediction error variations from the low values (matrix $\mathbf{Q}_0$) used in tuning the low-gain (non-adaptive) Kalman filter aimed at suppressing the estimator output y perturbations during quasi-steady-state intervals.

Figure 17 illustrates the effectiveness of averaging of drilling apparent power data by means of adaptive estimator implemented with original sampling time (T = 5 s). Estimator tuning has been carried out sequentially [56], i.e. the non-adaptive part of the estimator has been tuned first (through matrix $\mathbf{Q}_0$ choice), followed by adaptation mechanism (scaling factor γ_{ad}) tuning. The results show that in the case of notable power measurement fluctuations, the increase of estimator prediction error results in notable Kalman filter gains increase (illustrated by normalized gain vector Euclidean norm |**K**|). This, in turn, improves the averaged power tracking ability during highly-perturbed grid power profiles and large-magnitude transients. On the other hand, during quasi-steady-state intervals (characterized by low perturbation levels), the adaptive estimator is characterized by low gains, and behaves similarly to the non-adaptive estimator tuned for favorable suppression of perturbations in the averaged power estimate.

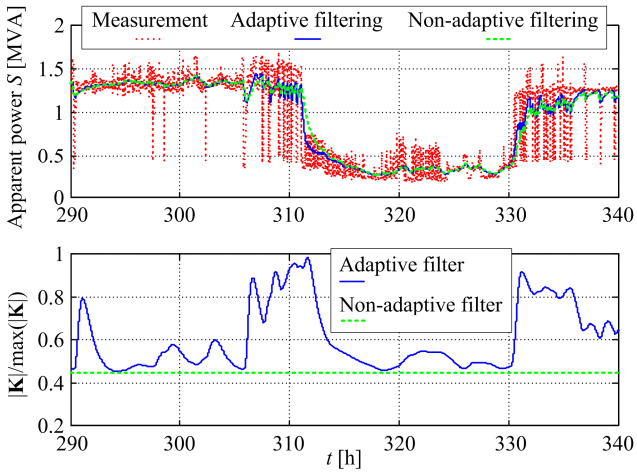

Figure 17. Illustration of effectiveness of adaptive Kalman filter-based power data averaging.

Appendix B: Battery model linearization and state-of-charge controller design

A brief derivation of the linearized battery power flow model is presented herein, aimed at designing a linear proportional (P) controller of battery state-of-charge presented in Section 4.

B.1. Battery power flow model linearization

For the purpose of state-of-charge controller design, the nonlinear battery model from equation (11) is linearized in the vicinity of the battery operating point (ξ_0, P_{b0}) by a first-order Taylor expansion:

$$\Delta\dot{\xi} = \frac{\partial f(\xi_0, P_{b0})}{\partial \xi}\Delta\xi + \frac{\partial f(\xi_0, P_{b0})}{\partial P_b}\Delta P_b \,. \tag{18}$$

where $\Delta\xi = \xi - \xi_0$ and $\Delta P_b = P_b - P_{b0}$ correspond to state-of-charge and battery power small-scale perturbations within model (18). For the sake of convenience, the above model may be rewritten in the following first-order lag term form:

$$\Delta\dot{\xi} + b \cdot \Delta\xi = K_p \cdot \Delta P_b \,. \tag{19}$$

where the linearized model parameters (damping parameter b and gain K_p) are given as follows:

$$b = -\frac{\partial f(\xi_0, P_{b0})}{\partial \xi} = \frac{1}{2Q_b R_s(\xi_0, P_{b0})}\left[1 - \frac{U_{oc}(\xi_0)}{\sqrt{U_{oc}^2(\xi_0) - 4R_s(\xi_0, P_{b0})P_{b0}}}\right] \cdot \frac{\partial U_{oc}(\xi_0)}{\partial \xi} + \frac{1}{2Q_b R_s(\xi_0, P_{b0})}\left[\frac{2P_{b0}}{\sqrt{U_{oc}^2(\xi_0) - 4R_s(\xi_0, P_{b0})P_{b0}}} + \frac{\sqrt{U_{oc}^2(\xi_0) - 4R_s(\xi_0, P_{b0})P_{b0}} - U_{oc}(\xi_0)}{R_s(\xi_0, P_{b0})}\right] \cdot \frac{\partial R_s(\xi_0, P_{b0})}{\partial \xi}, \tag{20}$$

$$K_p = \frac{\partial f(\xi_0, P_{b0})}{\partial P_b} = \frac{-1}{Q_b\sqrt{U_{oc}^2(\xi_0) - 4R_s(\xi_0, P_{b0})P_{b0}}} \,. \tag{21}$$

For the considered $LiFePO_4$ battery (see Fig. 9), the aforementioned linearized model parameter maps are shown in Fig. 18. Linearized model parameter variations are not emphasized, especially in the case of damping parameter b, which takes on rather small (near-zero) values. In particular, the $LiFePO_4$ battery open-circuit voltage U_{oc} and internal resistance R_s changes are only emphasized for fully-charged ($\xi_0 \to 100\%$) and deeply discharged battery ($\xi_0 \to 0$). Hence, the dominant battery charging dynamics could be approximated by a pure integral action under most operating regimes:

$$\Delta\xi \approx K_p \int_0^\tau \Delta P_b dt \,. \tag{22}$$

Moreover, in the case of battery idling ($P_b \to 0$), the above model is characterized by the following gain parameter:

$$K_{p,idle} = \frac{-1}{Q_b U_{oc}(\xi_0)}, \tag{23}$$

which corresponds to battery model maximum absolute gain value $\max(|K_p|)$ encountered during charging process (see left-hand-side plot in Fig. 18). Hence, this value should provide a robust battery state-of-charge controller tuning.

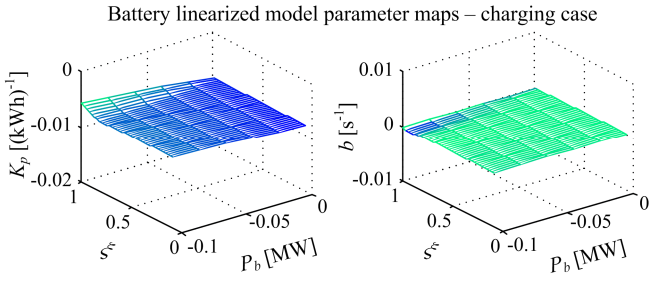

Figure 18. Battery linearized model parameter maps for anticipated range of charging operating regimes.

B.2. Charging controller design

For an integral-type battery process model (22), a proportional type (P) controller is sufficient to achieve steady-state accuracy of state-of-charge control. Figure 19 shows the block diagram of state-of-charge control system based on the linearized battery model (19), which also includes the equivalent delay $T_\Sigma = T_L + T_f + T_s/2$ due to grid inverter response lag (T_L), state-of-charge measurement lag (T_f) and sampling ($T_s/2$) in the case of discrete-time (digital) controller [57], and in the general case, a small-valued damping term b (dotted path in Fig. 19). Based on the block diagram in Fig. 19, the following closed-loop Laplacé s-domain transfer function model is obtained:

$$G_c(s) = \frac{\Delta\xi(s)}{\Delta\xi_R(s)} = \frac{K_\xi K_p}{K_\xi K_p + b + (1 + bT_\Sigma)s + T_\Sigma s^2}, \tag{24}$$

which can be simplified by neglecting the aforementioned rather small-valued damping factor b:

$$G_c(s) = \frac{1}{A_c(s)} = \frac{1}{1 + (K_\xi K_p)^{-1} s + (K_\xi K_p)^{-1} T_\Sigma s^2}. \tag{25}$$

The state-of-charge controller is tuned by matching the coefficients of the closed-loop transfer function (25) with the prototype second-order model transfer function:

$$G_c(s) = \frac{1}{1 + 2\zeta_n \Omega_n^{-1} s + \Omega_n^{-2} s^2}, \tag{26}$$

characterized by the damping ratio ζ_n and bandwidth Ω_n. By equating the coefficients of characteristic polynomials in equations (25) and (26) following expressions for the controller gain K_ξ and closed-loop bandwidth Ω_n are obtained:

$$K_\xi = \frac{1}{4\zeta_n^2 T_\Sigma K_p}, \tag{27}$$

$$\Omega_n = \frac{1}{2\zeta_n T_\Sigma}. \tag{28}$$

Since the charging controller should avoid response overshoot (i.e. in order to prevent entering discharging mode), the damping ratio ζ_n should be chosen larger or equal to unit value ($\zeta_n \geq 1$). This yields the following inequality relationship for the proportional controller gain absolute value which guarantees overshoot-free closed-loop behavior:

$$K_\xi K_p \leq \frac{1}{4T_\Sigma}. \tag{29}$$

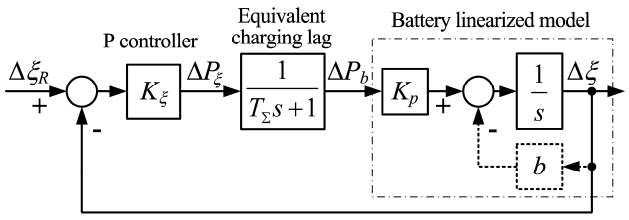

Figure 19. Block diagram of linearized battery state-of-charge control loop.